

Supplementary Materials for

**Integration mapping of cardiac fibroblast single-cell transcriptomes
elucidates cellular principles of fibrosis in diverse pathologies**

Ralph Patrick *et al.*

Corresponding author: Ralph Patrick, ralph.patrick@imb.uq.edu.au; Richard P. Harvey, r.harvey@victorchang.edu.au

Sci. Adv. **10**, eadk8501 (2024)
DOI: 10.1126/sciadv.adk8501

The PDF file includes:

Supplementary Text
Figs. S1 to S20
Legends for tables S1 to S10
References

Other Supplementary Material for this manuscript includes the following:

Tables S1 to S10

Supplementary Text

Extended methods

Conventional echocardiography and Doppler imaging

Transthoracic echocardiography was performed using a VisualSonics Vevo 2100 system equipped with MS400 transducer (FUJIFILM VisualSonics, Canada). Anaesthesia was induced by 5% isoflurane and confirmed by lack of response to firm pressure on one of the hind paws. During the ultrasound acquisition—under body-temperature-controlled conditions—isoflurane was reduced to 1.0–1.5% and adjusted to maintain a heart rate in the range between 460 – 500 beats per min. LVEF and other indices of systolic function were obtained from short-axis B-mode scans at the midventricular level, as described (129). The areas boarded by the endocardium were planimetrically measured on all four SAX images at end diastole and end systole, and from this a modified Bullet formula was used to derive left ventricular ejection fraction (LVEF) (left ventricular volume [LVvol] = length [L] x mean endocardial area x 5/6). All parameters were measured at least three times, and means are presented.

Speckle-tracking echocardiography and strain analysis B-mode traces acquired from the parasternal long-axis view were used to calculate global strain in longitudinal dimensions using *Vevo Strain* software (FUJIFILM VisualSonics, Canada) and a speckle-tracking algorithm, as described (78).

Tail-cuff blood pressure recordings

Systolic blood pressure was measured noninvasively in conscious mice using the tail-cuff method and a CODA instrument (Kent Scientific, CT, USA). Mice were placed in individual holders on a temperature-controlled platform (37°C) and recordings were performed under steady-state conditions. Before testing, all mice were trained to become accustomed to short term restraint for a week prior. Blood pressure was recorded for at least four consecutive days and readings were averaged from ten measurements per session.

Histology, immunofluorescence staining and confocal microscopy

All samples were processed in parallel under identical conditions for comparisons. Most procedures were performed as described (8), except for skin and healthy ventricle tissue sections in which modifications were incorporated (see Supplementary Materials). Briefly, tissue samples were fixed in 4% PFA, rinsed in PBS, and immersed in PBS containing 30% sucrose at 4°C before being embedded in optimal cutting temperature compound (OCT) for cryosectioning. Sections were incubated in blocking buffer for 1 hour and then were incubated in primary antibodies diluted in blocking buffer overnight at 4°C followed by wash and incubation in appropriate fluorophore-conjugated secondary antibodies diluted in blocking buffer for 1 hour at room temperature. Sections were then washed and mounted in a mounting medium containing DAPI. IF images were captured using LSM900 Inverted confocal laser scanning microscope. For Picosirius red staining, measurement of cardiomyocyte size and vessel density analysis, hearts were embedded in paraffin and later deparaffinized using standard protocols, and images were acquired using Olympus VS120 Slide Scanner. Primary antibodies and dilutions: PDGFR α (R&DSystems, USA; #AF1062, 1:100), DPPIV/CD26 (R&DSystems, USA; #AF954, 1:100), α -SMA (Sigma Aldrich, USA; #A5228, 1:400), α -SMA-Cy3 (Sigma-Aldrich, USA; #C6198, 1:250), Cardiac Troponin T-

Alexa Fluor 647 (BD Biosciences Pharmingen, USA; #565744, 1:100), Wheat Germ Agglutinin (WGA)-Alexa Fluor 647 (ThermoFisher, USA; #W32466, 1:100) and Isolectin B4 (IB4)-Alexa Fluor 488 (ThermoFisher, USA; #I21411, 1:100). All secondary antibody dilutions were 1:500.

Skin and mid-ventricle histology and staining

For isolating flank skin and ventricle mid-sections, 4-month-old adult male *Pdgfra^{eGFP/+}* knock-in mice were anaesthetised by intraperitoneal injection of ketamine (100 mg/kg) and xylazine (20 mg/kg) and perfused via left ventricular cardiac puncture with 30 mL of PBS1X at a flow rate of 3 mL/min (Legato 100 Syringe Pump, Becton Dickinson Plasti-plak 50ml, & Nipro 25G catheter needle). The mice were again perfused with 30 mL of 4% PFA and collected hearts and shaved flank skin samples were fixed with 4% PFA (4% PFA in PBS, pH 7.4) for 3-hours at room temperature. Fixed tissues were washed briefly in PBS1x (three times, 5 min each wash) and then dehydrated with 30% sucrose solution over-night at room temperature. Hearts were cut at the axial midline and these halves were embedded side-by-side in Tissue-Tek Optimal Cutting Temperature mounting medium (O.C.T., Tissue-Tek, Sakura) and stored at -80°C. Heart sections were cut in the axial orientation on a Leica CM1950 clinical cryostat (Leica Biosystems) at 7-μm thickness and collected onto Trajan Series 2 Adhesive slides (Trajan Scientific & Medical). Flank skin samples was embedded and cut in the same manner, at transverse orientation with nitrocellulose membrane acting as a structural support. For indirect immunofluorescence staining, tissue sections were permeabilized in 1× saponin-based permeabilization and wash buffer (0.2% (w/v) saponin containing 4% (v/v) FBS (v/v), 1% (w/v) BSA and 0.02% (v/v) Sodium Azide in PBS) for 15 min. Tissues were then stained over-night at 4°C in 1× saponin-based permeabilization and wash buffer using anti-Mouse DPPIV/CD26 Antibody (DPP4 polyclonal goat IgG, cat. no. AF954, 1:100 dilution), alpha-smooth muscle actin (α-SMA)-Cy3 (1:250 dilution, clone 1A4, Cat. No. C6198, Sigma-Aldrich), and Alexa Fluor® 647 Mouse Anti-Cardiac Troponin T (BD Pharmingen, cat. no. 565744, AB_2739341, Clone 13-11, 1:100 dilution). Following brief washing in PBS1x (3X 5 min washes), DPP4 stained sections were counterstained with suitable species-specific secondary antibody coupled to Alexa Fluor dye (1:500, Donkey anti-Goat IgG (H+L) Cross-Adsorbed Secondary Antibody, Alexa Fluor 633) diluted in 1× saponin-based permeabilization and wash buffer for 2-hours at room temperature. Sections were washed again in 1X PBS (3X 5 min washes), and stained with Vybrant™ DyeCycle™ Violet (ThermoFisher, Cat# V35003) at 1μM for 10 minutes in 1× saponin-based permeabilization and wash buffer, washed once with PBS1x and mounted under coverslip (Menzel-Gläser, 22x22 mm, #0). Dako fluorescent mounting medium (Agilent, Cat# S3023) was applied to the slides prior mounting and imaging. The endogenous fluorescence of eGFP was detected.

Confocal laser-scanning microscopy and image processing

z-stack high-resolution confocal microscopy of stained sections was performed using a LSM900 Inverted confocal laser scanning microscope that comprises an upright Zeiss Axio Observer 7, four laser lines, two Gallium Arsenide Phosphide photomultiplier tubes (GaAsP-PMT), and a motorised stage. Confocal tiling scan was employed using a ×10 objective, 0.45 numerical aperture 512 μm × 512 μm, WD 2.0, Plan-APO UV-VIS-NIR, and PBS immersion. For DPP4 z-stack imaging, we used a ×63 objective, 1.4 numerical aperture with a z-step size of 1 μm, 2,048 μm × 2,048 μm, WD 0.19, Plan-APO DIC-UV-VIS-IR, and oil immersion (Immersol 518 F, Refractive Index: 1.518, Zeiss). Whenever comparisons were made, the settings for confocal scanner detection and laser excitation were kept identical between samples. Z-stacks were processed using

Fiji software (ImageJ2, V2.14.0/1.54f), and finally, distinct LUTs were applied to each image to improve the visibility of the different channels.

Cardiomyocyte size and vessel density analysis

To analyse cardiomyocyte size (as a surrogate measure of hypertrophy) and vessel density, ventricle sections stained with WGA and IB4 were imaged at 40x objective magnification and analysed as previously described (130). Pre-processing was carried out using *ImageJ* followed by analysis of cardiomyocyte size and vessel density on *CellProfiler* (v4.2.4). Cardiomyocyte size was normalised to the normal chow control group whilst vessel density was calculated as number of vessels per cardiomyocyte and normalised to the normal chow control group.

Measurement of lung weight

Ratio of wet to dry lung weight was estimated as described previously (78).

Volcano plot and GO term analysis

For proteomics, volcano plots were generated using the *RStudio* package *EnhancedVolcano*. Data generated during differential expression analysis of proteins in HFP EF vs Chow mice was plotted using cut offs of 0.5 for fold change and 0.05 for adjusted *p*-value. Downregulated and upregulated proteins were then run separately through the Database for Annotation, Visualisation, and Integrated Discovery (*DAVID*, david.ncifcrf.gov), using the preselected databases for pathway analysis. Both up and downregulated pathways were visualised together using *RStudio* package *ggplot2*, with the number of DE genes present in that pathway represented by circle size, with adjusted *p*-value (Benjamini<0.05) represented by a spectrum colour range.

Cell Isolation

Total interstitial cell population (TIP) were isolated as previously described (8). Briefly, hearts were minced and incubated in collagenase type II (Worthington) at 37°C before filtering through 40 mm strainers. Cells were resuspended in red cell lysis buffer, followed by dead cell removal, immunostaining for 15min on ice with indicated fluorophore-conjugated antibodies and two times wash with fluorescence-activated cell sorting (FACS) buffer (2% FBS, 2mM EDTA in PBS, pH 7.4) before the acquisition.

Flow Cytometry

FSC-H versus FSC-A, FSC-H versus FSC-W and SSC-H versus SSC-W cytograms were used to discriminate and gate out doublets/cell aggregates during sorting or analysis. DAPI was used to distinguish live (DAPI-) and dead (DAPI+) cells. For most samples, at least 10,000 final gate events were collected and stored. Flow cytometry experiments were performed on a Canto II (BD Biosciences, USA), using *FACSDiva* software (BD Biosciences, USA). Lineage negative (CD31-/CD45⁻) *Pdgfra*-eGFP⁺ CF flow cytometry was performed using a BD FACSsymphony A5. FACS analysis was performed using *FlowJo* software (version 10.8.1, BD). For details of DPP4, SCA-1, CD90.2 and CD55 staining in live CD31-/CD45⁻ *Pdgfra*-eGFP⁺ CF, flow cytometry events, and further gating, see Supplementary Material. Antibodies and dilutions: Fc Block (CD16/32) (BioLegend, USA; #101301, 1:400), Ly-6A/E (SCA-1)-APC/Cy7 (BD Biosciences Pharmingen, USA; # 560654, 1:400), CD90.2 (Thy1.2)-APC/Cy7, (BioLegend, USA; # 105327, 1:200), CD26 (DPP4)-APC (BioLegend, USA; # 137807, 1:100), CD55-PE REAfinity (Miltenyi Biotech, USA; # 130-104-055, 1:40), BD OptiBuild™ BUV395 Rat Anti-Mouse CD31 (BD Biosciences

Pharmingen, USA; Clone 390, 1:400), CD45-BV786 (BD Biosciences Pharmingen, USA; # 564225, Clone 30-F11, 1:400), CD45-APC/Cy7 (BD Biosciences Pharmingen, USA; # 557659, 1:400).

Heart ventricle cell isolation and high-speed flow cytometry of live *Pdgfra-eGFP*⁺ CF

Two-step digestion of heart tissue for cellular isolation was performed as described before with few modifications (131). Hearts of 4-month-old adult male *Pdgfra*^{eGFP/+} knock-in mice were carefully dissected, washed in ice-cold DMEM, ventricles were further separated transversally, and cut into small pieces with blades until a homogeneous, paste-like slurry was formed. Seven ml of digestion solution containing collagenase type II (265 Unit/mL, Worthington, DC, United States), 0.5 U of Dispase (Cat. No. 07913, STEMCELL Technologies, Canada), 0.05 mg/mL of DNaseI (Cat. No. 10104159001, Roche/Sigma-Aldrich, 100 mg from bovine), and 1% BSA (Sigma-Aldrich Pty Ltd., A3311-50G) dissolved in DMEM (Cat. No. 10566016) was added and the preparation was placed on a water bath with constant rotation at 37°C for 40 min. After 20 min of incubation, 10 mL of FACS buffer was added to the ventricle preparations and the homogenate was gently pipetted up and down 10 times to enhance dissociation with a 10 mL serological Stripette® on ice. Ice-cold FACS buffer was added to make the final volume up to 20 mL volume and the supernatant was then passed sequentially through 100 µm and 70 µm cell strainers. The remaining non-digested pellet was incubated with additional 4 mL of digestion buffer (detailed above) for another 20 min in a water bath. The first filtered preparation was centrifuged at 600 g for 6 min at 4°C, and the flicked pellet was resuspended in 5 mL of ACK lysing buffer (i.e., red blood cell lysis buffer in w/v) (potassium carbonate 0.01%, ammonium chloride 0.083%, and EDTA 0.0004% in H₂O at pH 7.4) and further incubated for 3 min. Then, 20 mL of FACS buffer was added to stop the lysis and cell pelleting was carried out as described before. After flicking, 5 mL of FACS was added to the cell and kept on ice. After further digestion of the remaining non-digested pellet, the cells were collected as described above for the first dissociation step. At the end of the process, the two dissociated cell mixtures were pooled together in 10 mL of FACS buffer, which was further divided into 1.5 mL tubes, cells pelleted at 600 g for 5 min at 4°C and flow cytometry staining was carried out in 400 µL of FACS buffer, after the mixture was incubated with Fc block antibody for 15 min on ice.

Each sample was ran using a BD FACSymphony A5 high-speed cell analyser, with 2 million total events captured, and at least thousand *Pdgfra-eGFP*⁺ CF being analysed. Flow cytometry measurements were run at a mid-flow rate, and the core stream allowed to stabilize for 5 s prior acquisition. Flow cytometry of resting and live lineage-negative (CD31⁻/CD45⁻) *Pdgfra-eGFP*⁺ ventricular CF was performed after staining with specific antibodies detailed in the main text, and DAPI negative cells were selected and gated for eGFP fluorescence. Unstained and isotype controls were used in each combination for DPP4-APC, SCA-1-APC/Cy7, CD90.2-APC/Cy7, and CD55-PE. Fluorescence data was collected and further compensated using FacsDIVA 8 software. Fluorescence data was analysed after biexponential transformation in FlowJo Portal (version 10.8.1, Becton Dickinson & Company (BD)) using Mac OS X operating system.

Cell/nuclear isolation and sequencing - HFpEF model

For the HFpEF model, we adapted a protocol for simultaneous isolation of CM nuclei and non-myocyte cells, as previously described (63). TIP cells were isolated as above. For CM nuclei extraction, strainers were washed with FACS buffer to collect cardiomyocyte in a 50-ml Falcon

tube. After 2 rounds of centrifugation (500g x 5 min), CM nuclei were isolated by swelling CMs in a hypotonic solution (91 mM NaCl, 5.3 mM KCl, 0.5 mM MgCl₂, 0.293 mM CaCl₂, 10 mM glucose, 10 mM HEPES at pH 7.4 and 0.05% Triton-X-100 supplemented with 40 U/ μ l RNasin® Ribonuclease Inhibitor (Promega Corporation, WI, USA) before triturating cells using a 30-gauge hypodermic needle to mechanically fragment cells. Nuclei were then isolated by filtration through a 40 μ m cell strainer to exclude large debris. Finally, nuclei suspension was centrifuged at (500g x 5 min) before staining with DAPI, followed by FACS for isolation of nuclei. TIP cells and CM nuclei were FACS-isolated and subsequently pooled at specific proportions (50% TIP (without CD31⁺ cells), 20% CD31⁺ cells and 30% CM nuclei). Isolation of single cells was performed in two batches on separate days, with samples from each treatment group split across days to mitigate batch effects. Cells/nuclei from 2 mice were pooled together after FACS isolation and considered as one replicate and 2 replicates per condition were run for sequencing.

FACS was used to isolate CM nuclei from each heart and enumerated using a hemocytometer for single cell RNA sequencing workflows using a 10x Genomics platform. Approximately 6000 total nuclei (per condition) were loaded into each channel and captured on the 10x Genomics Chromium Controller using the Chromium Single Cell 3' v3.1 reagent kit. Following capture and reverse transcription, cDNA was synthesized and amplified, then final Illumina compatible sequencing libraries generated. Libraries were sequenced to an approximate depth of 30,000 reads per cell on an Illumina S4 flow cell, using the Illumina NovaSeq 6000 Sequencer. Isolation of single cells was performed in two batches on separate days, with samples from each treatment group split across days to mitigate batch effects.

Analysis of human spatial transcriptomic data - fibroblast clustering

First, we took the integrated mouse CF data and removed types F-WntX, IR, and F-IFNS. To relate the mouse and human genes, we used the orthogene package (version 1.6.1) to convert mouse genes into human homologues. We used the findMarkers function in the scran package (version 1.28.2) to identify genes that were significantly associated with each type with FDR-adjusted P-value < 0.05 and log fold-change > 0.25. Then, we downloaded the Kuppe and colleagues' snRNA-seq and Visium data (21), in the form of gene expression log-count matrices, from the publication's data availability URL. The Visium data had already been filtered to remove spots with no or low gene expression. For the Visium data we also extracted the spatial location information for each of the Visium resolved spots. For the snRNA-seq data, we restricted to cells that were annotated as Fibroblast, and kept only genes that were detected in at least 1% of cells. We selected 500 top highly variable genes and used these to perform multi-batch principal component analysis using the batchelor package (version 1.16.0), followed by batch correction according to the sequencing samples using the reduced mutual nearest neighbour approach in the batchelor package. We then performed unbiased clustering of these cells using the clusterRows function in the bluster package (version 1.10.0) using the two-step param approach, where the first step was K-means clustering with 500 centres, followed by louvain graph-based clustering over the 500 centres. We then performed k-nearest neighbour-based smoothing of the cluster labels with k=100 nearest neighbours. For visualisation, we performed further dimensionality reduction using UMAP via the runUMAP function in scater (version 1.28.0). We used the same strategy as the mouse data to identify genes significantly associated with each human fibroblast cluster. We used the topGO function in the limma package (version 3.56.2) to assess the significance of enrichment of gene ontology terms for each of the human fibroblast clusters. To assess the concordance of marker

genes among each mouse and human cluster, we calculated the Jaccard index of the identified genes for each pair of clusters and visualised this in a heatmap.

Analysis of human spatial transcriptomic data - MYO and MFC scores

We performed a differential expression analysis comparing the human fibroblast cluster H1 and H6 using the findMarkers function in the scran package, using genes that were detected in at least 20% of cells within H1 and H6. We had observed that several genes that were positive markers for cluster H1 were also markers of cardiomyocytes, thus, we performed an additional differential expression analysis between the cluster H1 and the snRNA-seq resolved cells that were annotated as Cardiomyocytes. To extract a MYO-specific score, we assigned a weighting to each gene corresponding to the log fold-change of cluster H1 compared to cluster H6 and reassigned the weighting to zero for genes with a log fold-change below 0.1 as well as for genes with a positive log fold-change for Cardiomyocyte cells versus cluster H1. To extract a MFC-specific score, we performed a similar weighting scheme with a log fold-change threshold of 0.5 and no further reassignment with Cardiomyocytes. To extract a score for each gene expression profile, we performed elementwise multiplication of each gene's expression with the weighting for the MYO and MFC identities respectively, both for the snRNA-seq resolved cells and for the Visium-resolved spots. We checked the MYO and MFC scores were highest among Fibroblasts by generating boxplots for all cell types within the snRNA-seq data. We visualised the MYO and MFC scores in the Visium data using bivariate colour plots for spots that were annotated as Fibroblast in the original publication. Finally, we calculated total MYO and MFC scores for each patient Visium sample by calculating the sum of each MYO and MFC score among Fibroblast spots and divided by the total number of spots identified.

Figure S1

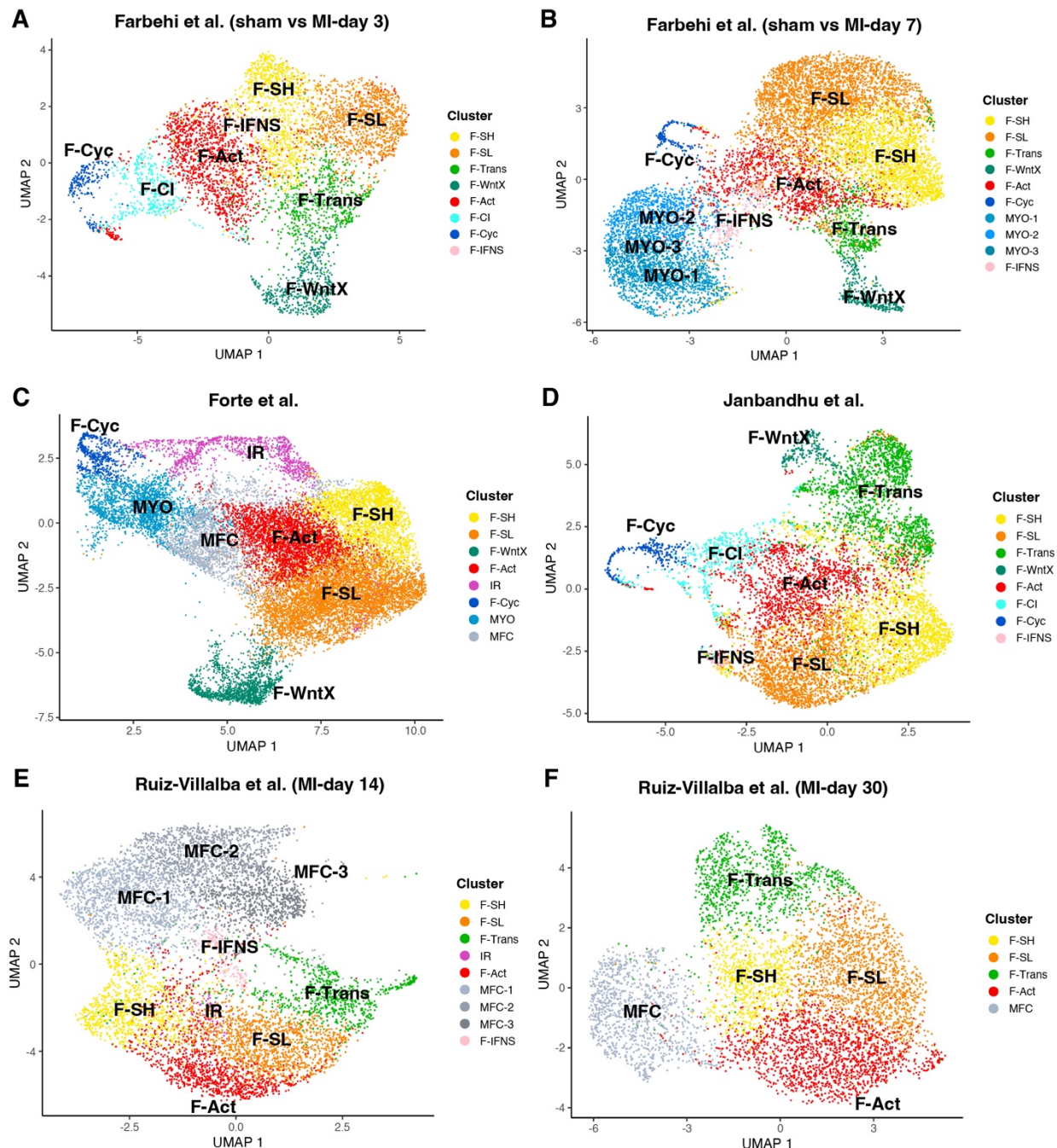


Fig. S1. Clustering and cell type assignments for the MI datasets included in the integration analysis. (A-F) Fibroblast sub-types were assigned based on marker genes in accordance with foundational scRNA-seq publications (see Table 1). (A) sham and MI-day 3. (B) sham and MI-day 7 data from Farbhei and colleagues utilising the cluster identifications from the original publication. (C) re-clustering analysis of uninjured and MI-days 1-28 data from and colleagues. (D) Sham and MI-day 3 data from Janbandhu and colleagues using the population identities from the original publication. Note this was derived using a label transfer analysis from (A). (E, F) Clustering of MI-day 14 (E) and MI-day 30 data (F) from Ruiz-Villalba and colleagues.

Figure S2

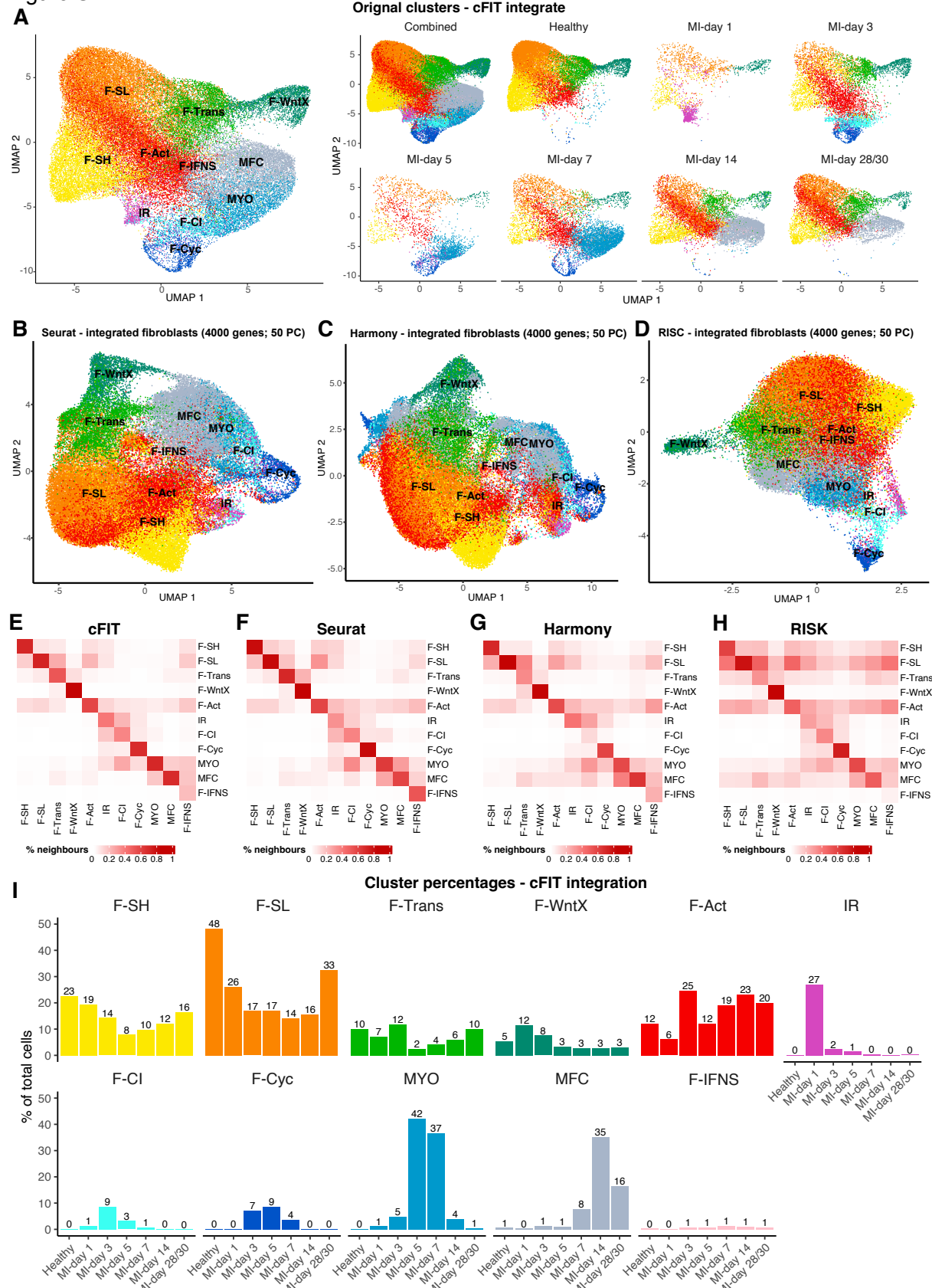


Fig. S2. Integration of fibroblasts across MI timepoints and datasets. (A) UMAP plot based on cFIT integration with cells coloured according to their dataset-specific cluster assignments. Shown is an aggregate of CFs across conditions or according to injury timepoint. (B-D) UMAP plots based on alternative integration approaches, (B) Seurat, (C) Harmony and (D) RISC. In all cases, the top 4000 variable genes were used as for the cFIT integration analysis, and the first 50 PCs. (E-H) Nearest neighbour analysis among the cell clusters for the indicated integration method. For each cluster (by column), the average percentage of nearest 200 neighbours among all clusters was determined. (I) Percentage of cells following cFIT integration in each population according to experimental condition.

Figure S3

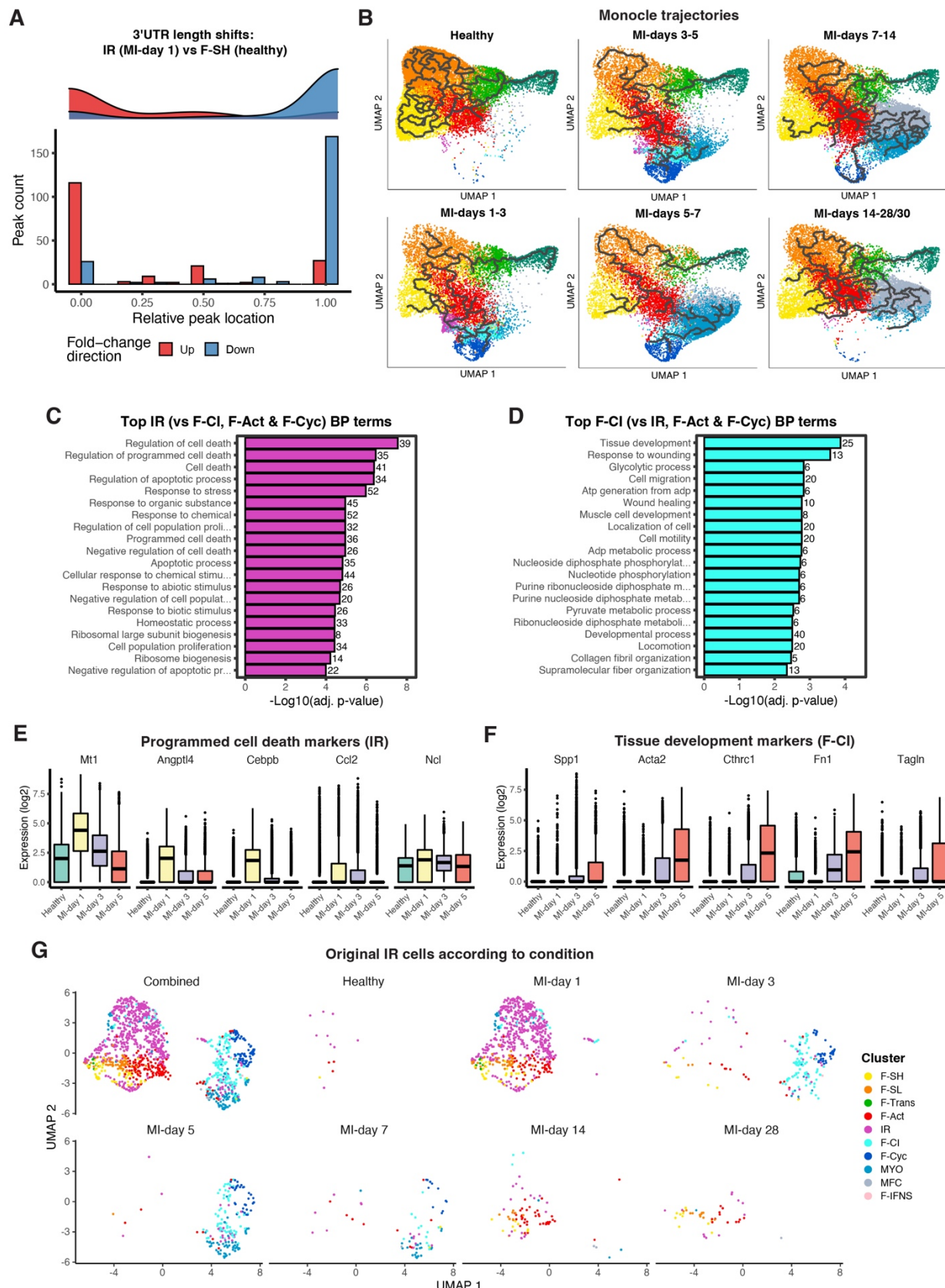


Fig. S3. Analysis of IR and F-CI cell populations. (A) Sierra plot of relative shifts in 3'UTR length between IR at MI-day 1 and F-SH from healthy hearts. (B) UMAP plot split according to successive pairs of MI time points in comparison to the combined healthy control, with *Monocle* trajectories overlaid on UMAP coordinates. (C,D) Top 20 GO Biological Process terms for DE genes upregulated (MAST testing; $p_{adj} < 1 \times 10^{-5}$; log₂ fold change > 0.5) in (C) IR compared to F-CI, F-Act and F-Cyc combined at MI-days 1 & 3 or (D) F-CI compared to IR, F-Act and F-Cyc combined at MI-days 1 & 3. (E) Gene expression across all fibroblasts by timepoint for representative genes from the *programmed cell death* GO term over-represented in genes upregulated in IR. (F) Gene expression across all fibroblasts by timepoint for representative genes from the *tissue development* GO term over-represented in genes upregulated in F-CI. (G) UMAP according to experimental condition of IR cells as identified by initial clustering of the Forte and colleagues' data (10), with updated cell labels following the kNN analysis incorporating all MI datasets.

Figure S4

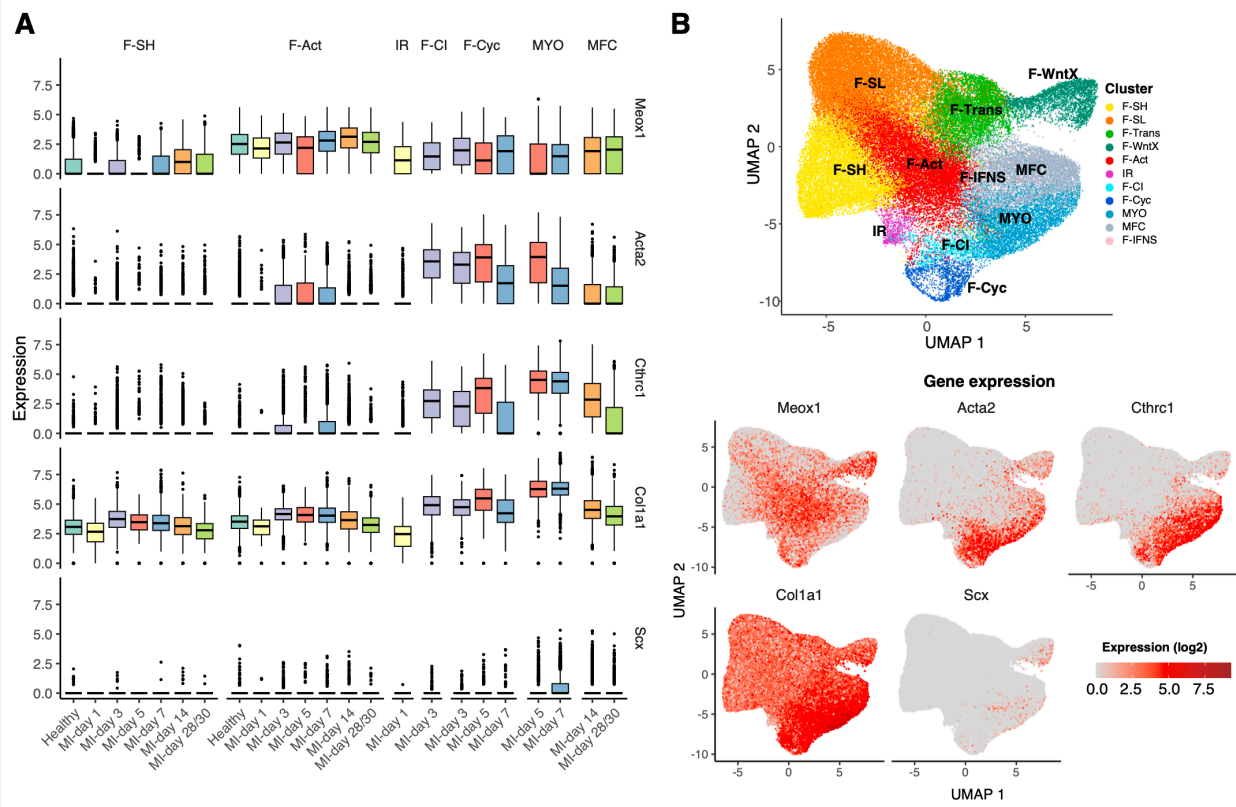


Fig. S4. Analysis of MI expression dynamics. (A) Expression of select fibroblast activation or myofibroblast markers across fibroblast sub-types at the indicated MI timepoint or uninjured control. (B) Expression of select fibroblast activation and myofibroblast markers in an aggregate of healthy and MI cells.

Figure S5

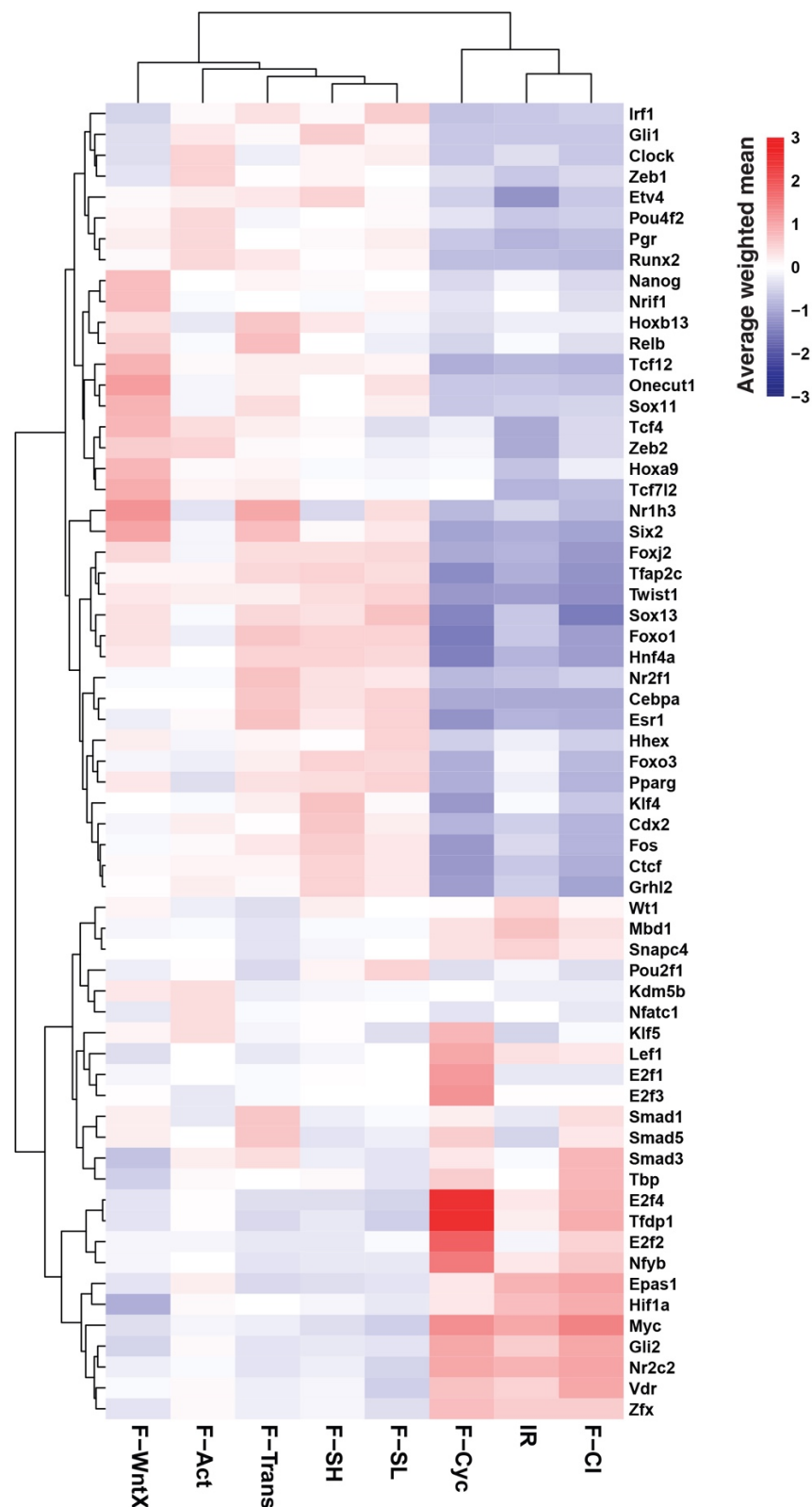


Fig. S5. Predicted TF regulators for MI-days 1-3. Top ten predicted TFs for each indicated population for MI-days 1-3 cells. Shown are the average weighted mean decoupleR scores across the cells for each population.

Figure S6

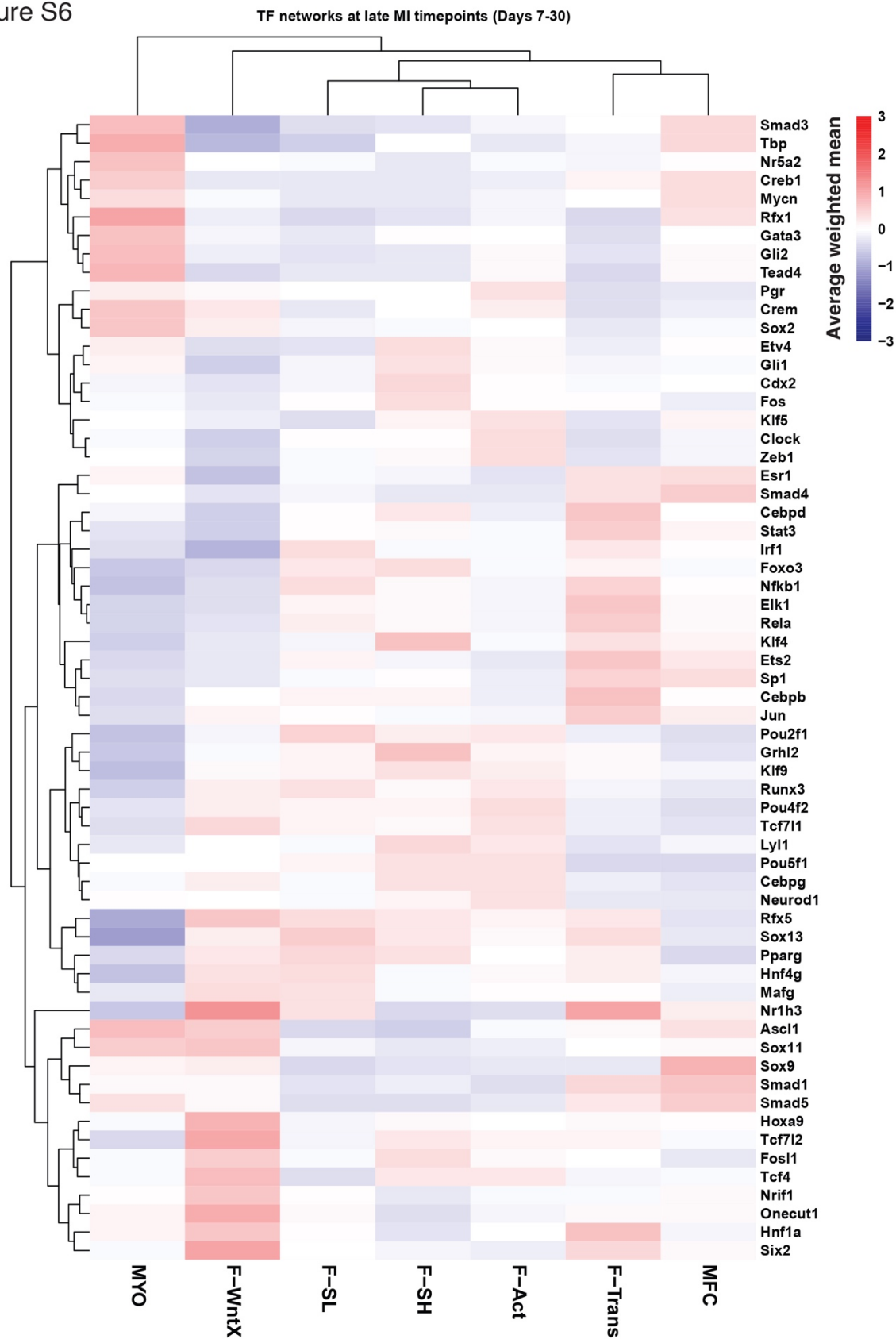


Fig. S6. Predicted TF regulators for MI-days 7-30. Top ten predicted TFs for each indicated population for MI-days 7-30 cells. Shown are the average weighted mean decoupleR scores across the cells for each population.

Figure S7

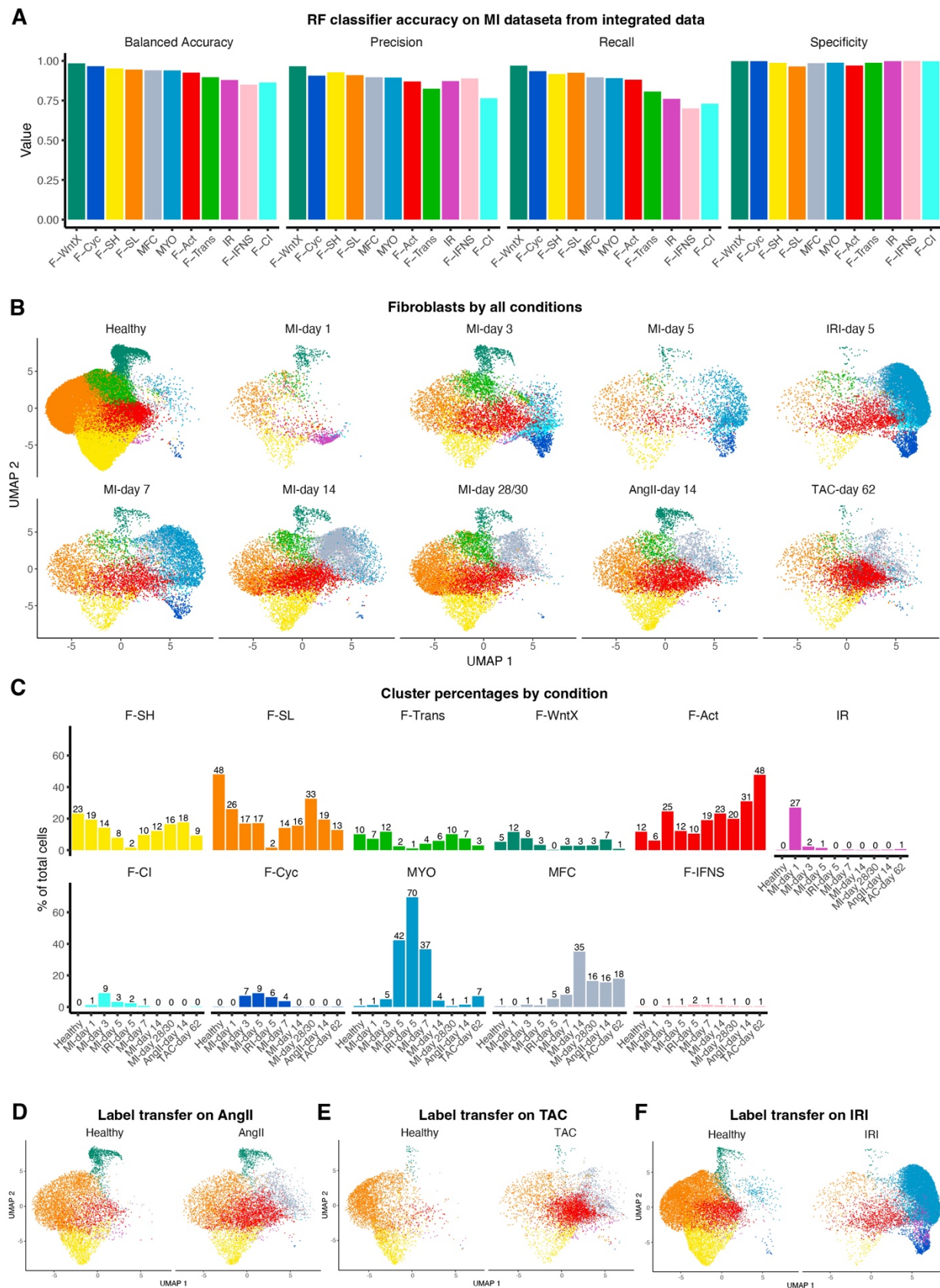


Fig. S7. Cross-disease integration of fibroblast datasets. (A) Prediction accuracy metrics for predicting fibroblast cell types from the integrated MI dataset using a Random Forest (RF) classifier. Evaluations are based on 10-fold cross-validation. (B) UMAP of cross-disease datasets and timepoints according to condition. Fibroblast cell types in the non-MI conditions predicted using the RF classifier. (C) Proportion of fibroblast cell types according to experimental condition and timepoint (D-F) Seurat label transfer analysis from the integrated MI dataset to cross-disease datasets (D) AngII, (E) TAC and (F) IRI.

Figure S8

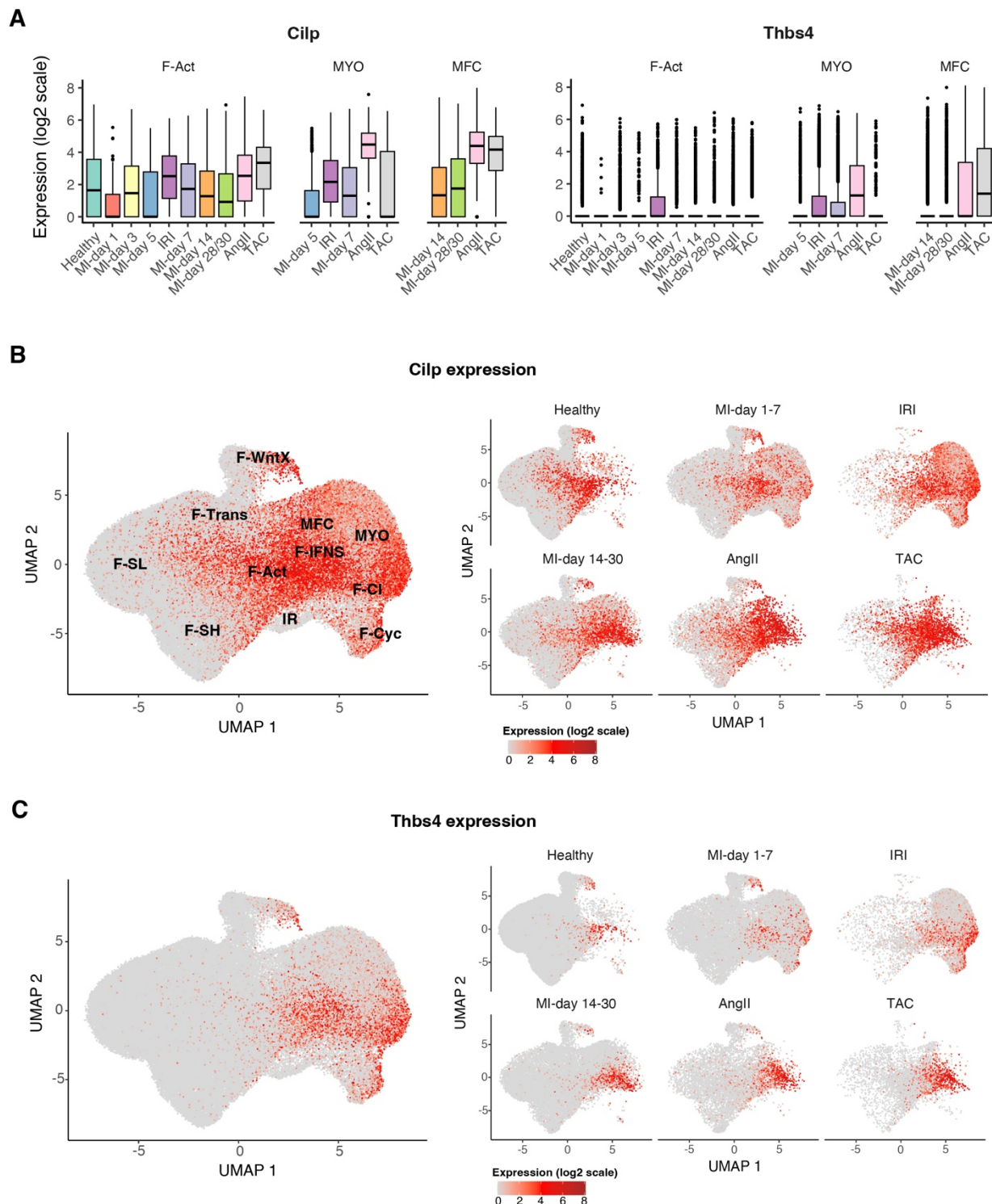


Fig. S8. *Cilp* and *Thbs4* expression in different CF subpopulations. (A) Box plots showing expression in F-Act, MYO and MFC. (B,C) UMAPs showing expression across an aggregate MI time course (including healthy hearts; left panels) alongside those for individual conditions.

Figure S9

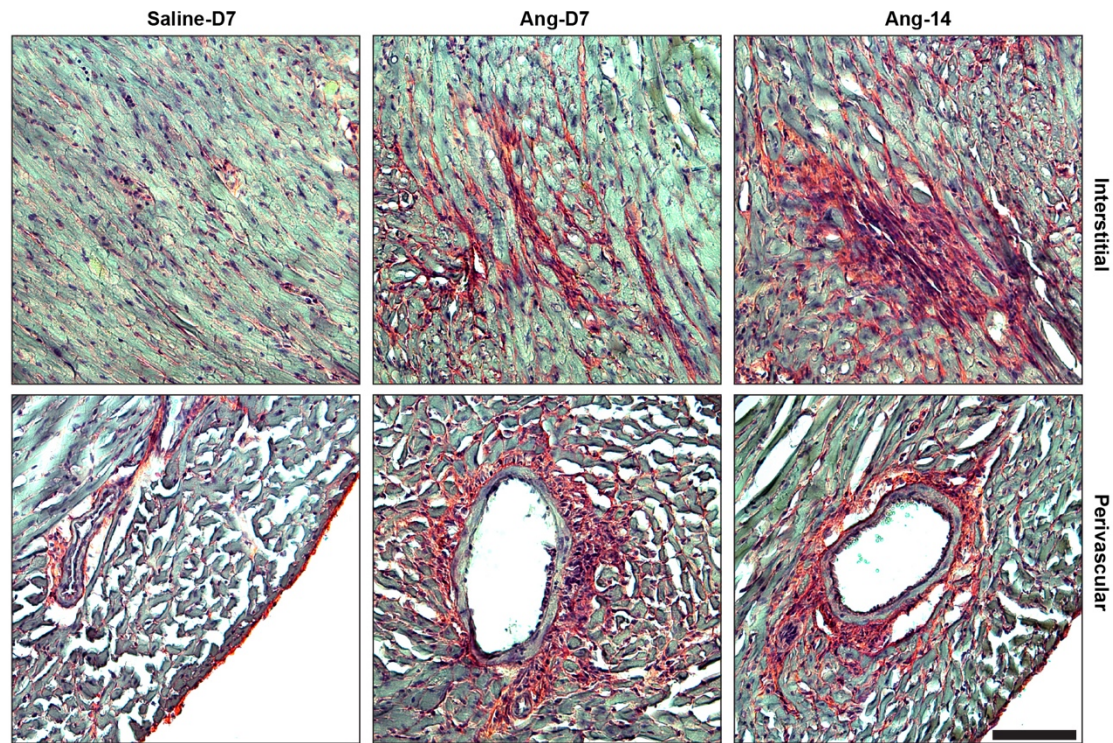


Fig. S9. Documentation of fibrosis in AngII model. Representative images of heart sections at indicated timepoints after AngII treatment showing collagen staining using Picrosirius red (n=3). Top panels – interstitial foci; bottom panels – perivascular foci. Scale bar, 100 μ m.

Figure S10

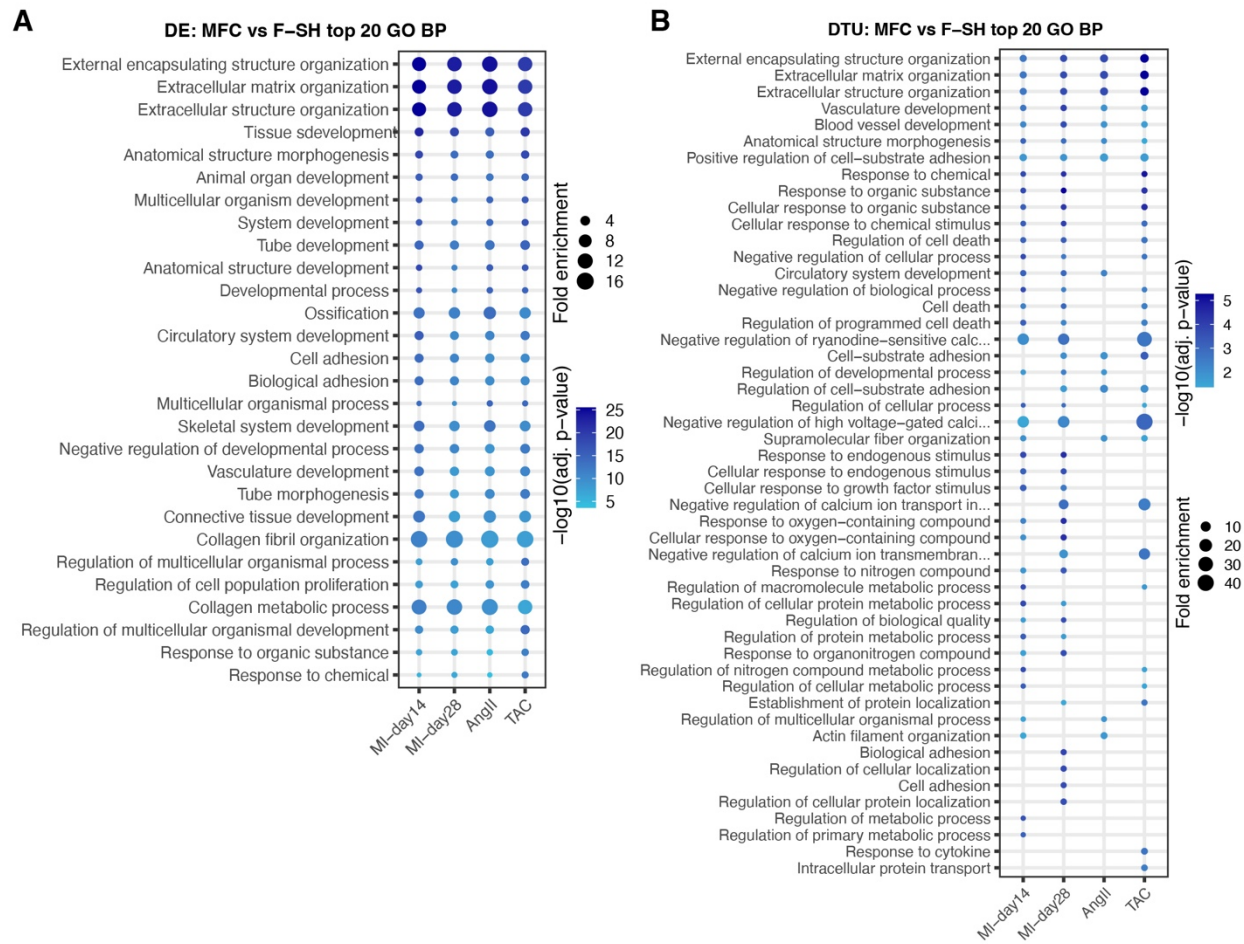


Fig. S10. Differential gene and transcript use in MFC. (A-B) Top 20 GO Biological Process terms for either (A) differentially expressed (DE) genes or (B) differential transcript use (DTU) genes comparing MFC from the indicated disease/timepoint to F-SH from healthy hearts.

Figure S11

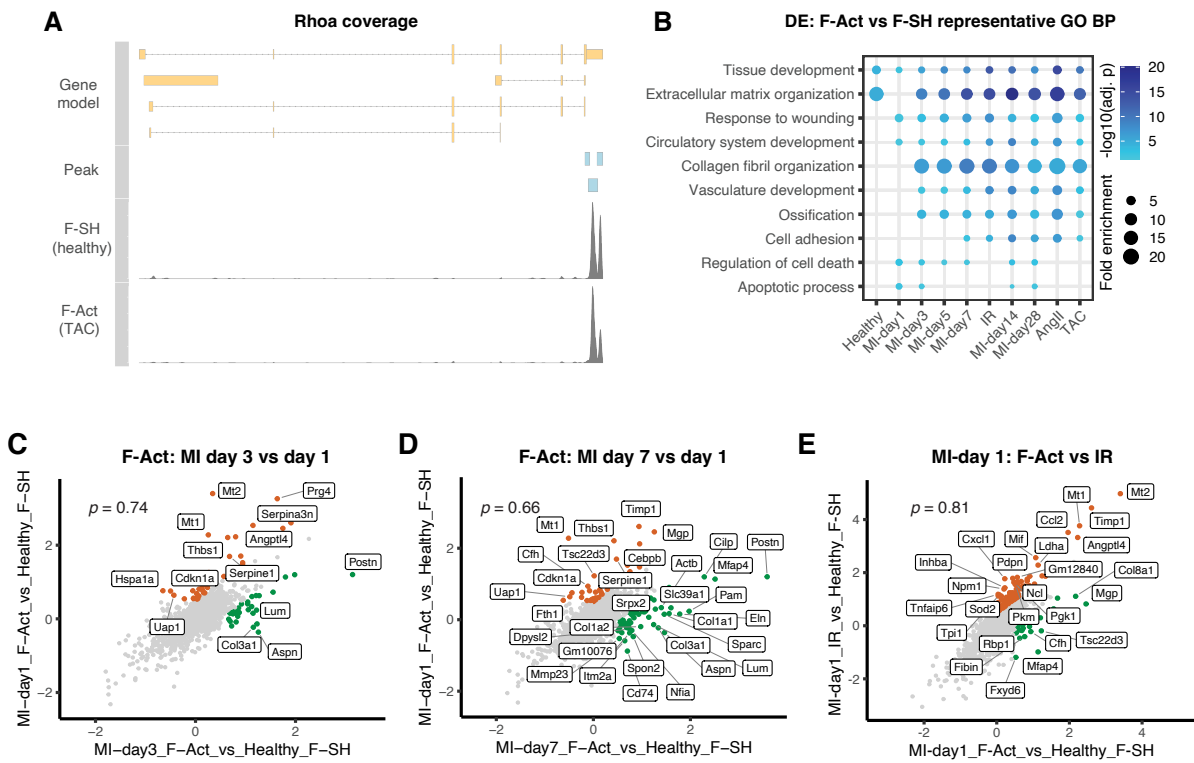


Fig. S11. Analysis of F-Act differential transcript use and gene expression across MI timepoints and disease conditions. (A) Read coverage plot for the *Rhoa* gene, with differential peaks indicated and comparing F-Act coverage from TAC to F-SH expression from the relevant control heart. (B) Representative GO terms comparing F-Act across conditions to F-SH cells from the relevant healthy heart data. (C,D) Comparison of Log₂ fold change differences in gene expression comparing F-Act to F-SH from healthy hearts for (C) F-Act at MI-day 3 vs MI-day 1 or (D) F-Act at MI-day 7 vs MI-day 1. (E) Comparison of Log₂ fold change differences in gene expression comparing F-Act (at MI-day 1) to F-SH against IR vs F-SH.

Figure S12

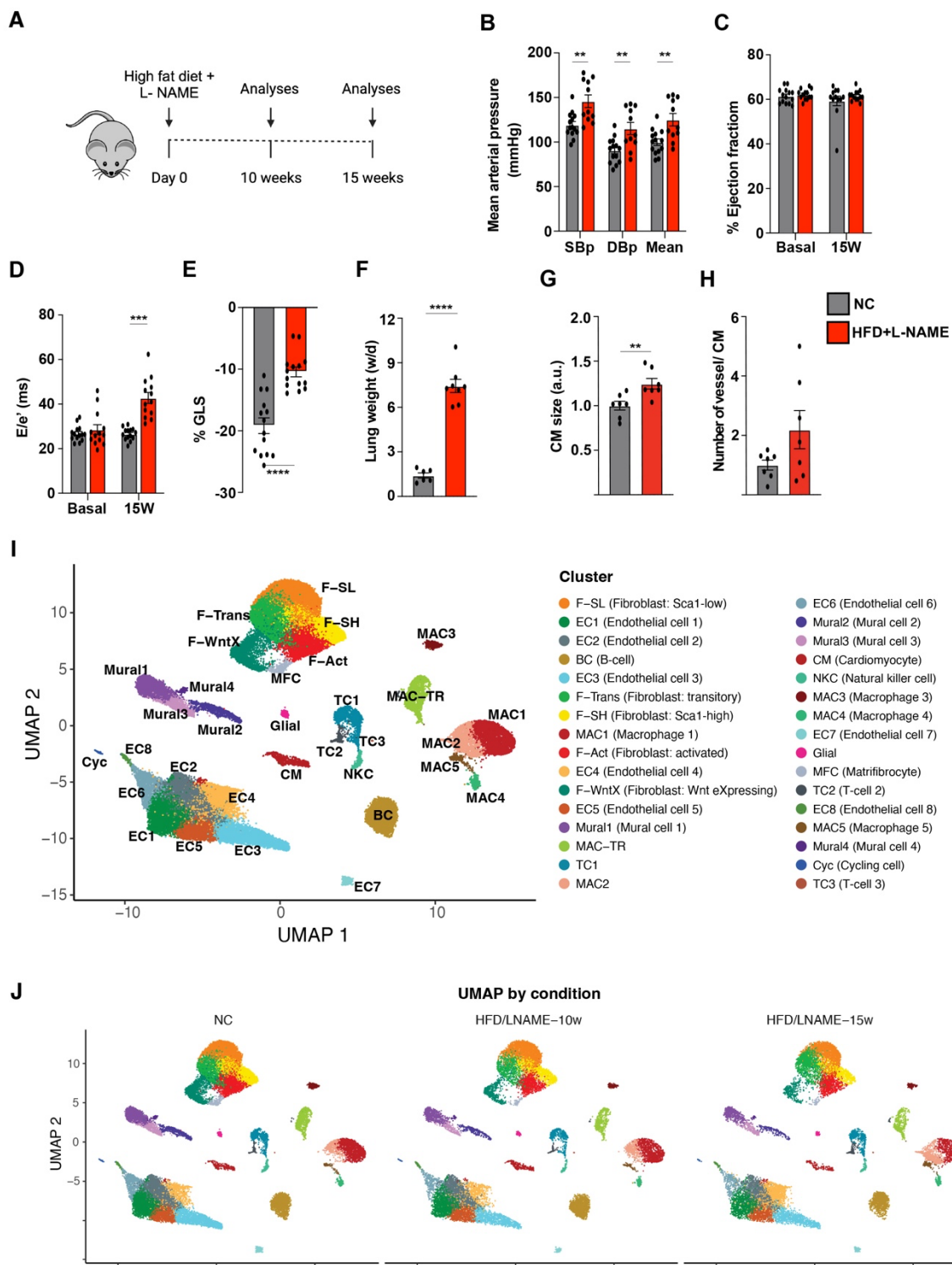


Fig. S12. Validation and scRNA-seq analysis of HFpEF mice model. (A) Schematic of the experimental design. (B) Systolic (Sbp) and Diastolic blood pressure (Dbp) of experimental groups after fifteen weeks of treatment (n=14 normal chow; n=11 HFD + L-NAME). (C) Percent left ventricular ejection fraction. (D) Ratio of mitral valve E wave to e' wave (E/e'). (E) LV global longitudinal strain (GLS) (B-D n=14 normal chow; n=13 HFD+ L-NAME). (F) Ratio of wet to dry lung weight (LW) (n=6 normal chow; n=8 HFD +L-NAME). (G) Quantification of IF staining shown in Figure S13A for cardiomyocyte area. Values are normalized to normal chow-mice (n=7). (H) Quantification of IF staining shown in Figure S13A for number of capillaries. Values are normalized to normal chow-mice (n=7). (I) Aggregate UMAP showing identified cell types from clustering. (J) UMAP according to condition. *p < 0.05, **p < 0.01, and ***p < 0.001.

Figure S13

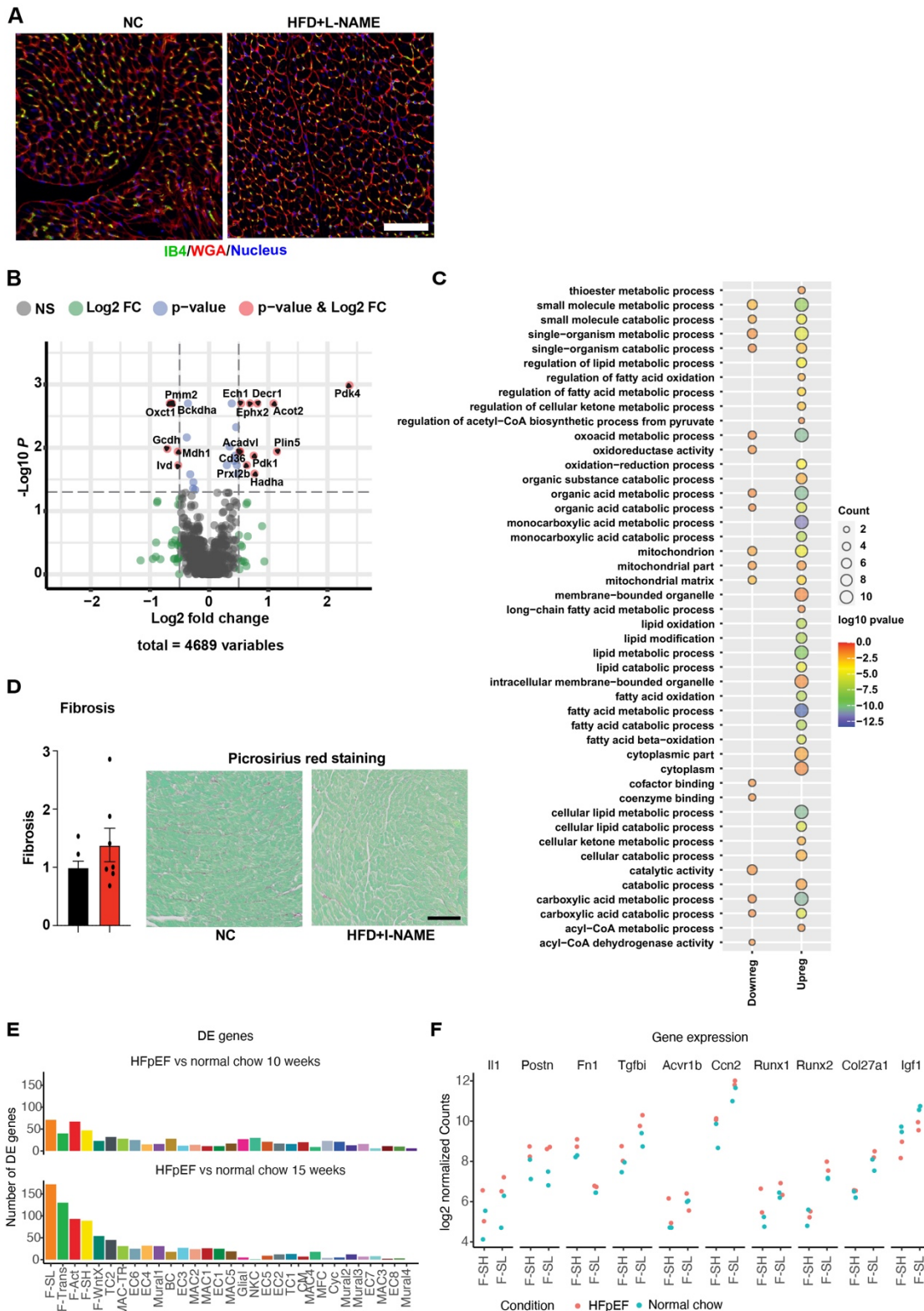


Fig. S13. Vascular density, proteomics and fibrosis analysis in the murine HFpEF model. (A) Representative IF images of wheat germ agglutinin (WGA) and isolectin B4 (IB4)-stained heart sections from HFD+L-NAME and normal chow mice. Scale bar, 100 μ m. (B) Volcano plot illustrating the distribution of all proteins identified with Tandem Mass Tagged (TMT) discovery proteomics on HFD+L-NAME vs normal chow hearts. (C) Gene Ontology (GO) term analysis on significantly upregulated and downregulated proteins in HFD+L-NAME vs normal chow hearts. (D) Representative images of heart sections showing Picosirius red and fast green staining. Quantification is shown on the left ($n=7$). Scale bar, 100 μ m. (E) Counts of the number of differentially expressed genes (DESeq2; adj. $p < 0.05$ and Log₂ fold-change > 0.5) between HFpEF and normal chow-fed mice at 10 weeks or 15 weeks of HFD + L-NAME. (F) Expression of select differentially expressed genes. Shown are Log₂ normalised pseudo bulk counts for the biological replicates ($n = 2$ per condition).

Figure S14

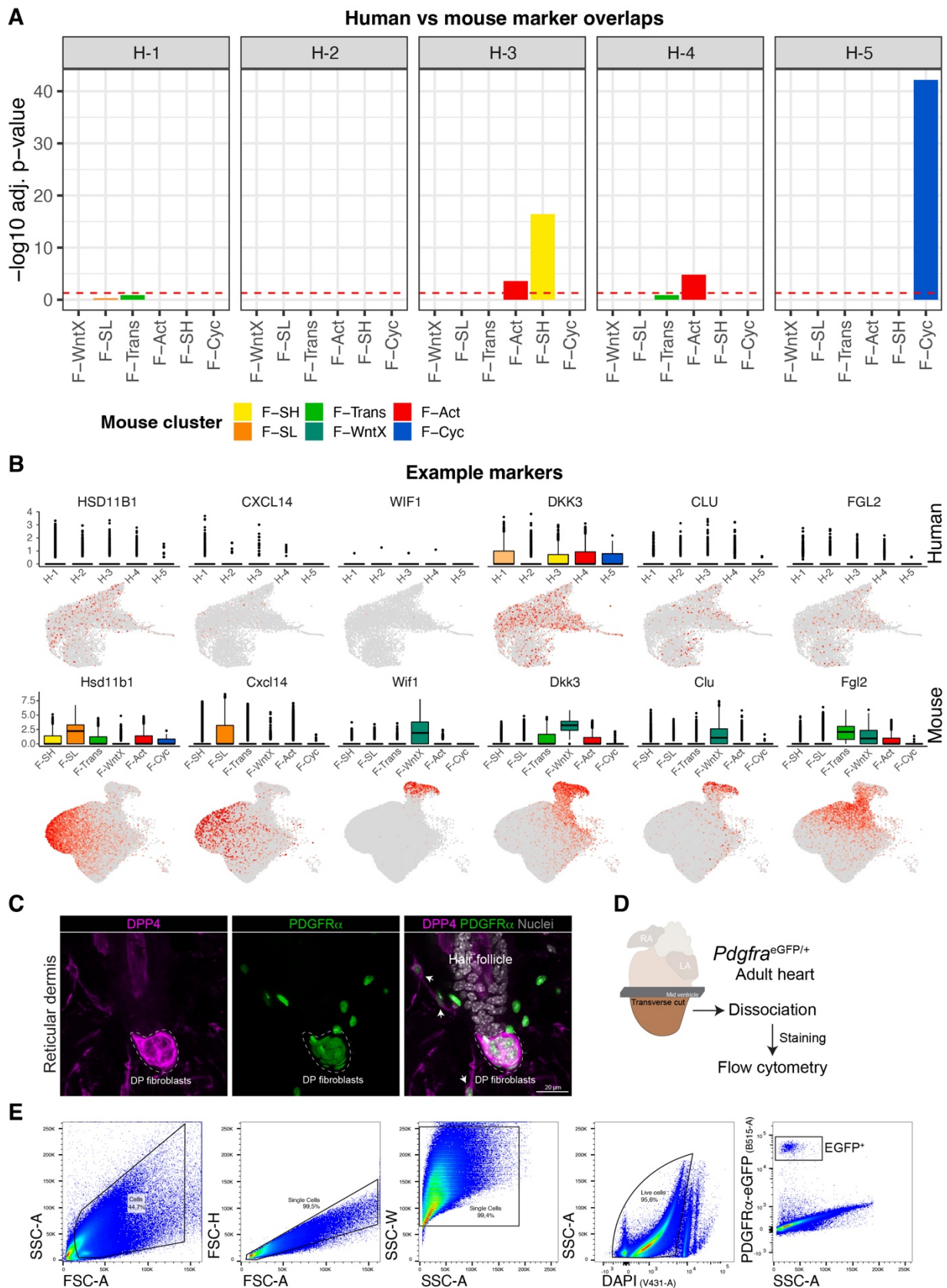


Fig. S14. Comparison of mouse with human fibroblast states. (A) Overlap of marker genes for each of the fibroblast clusters from healthy human hearts (70) compared to the fibroblast cell types defined in mouse. Indicated are adjusted *p*-values from Fisher's exact tests. (B) Example marker genes from key mouse fibroblast cell types as visualised in human (top) or mouse (bottom) cells in healthy hearts. (C) 24 μ m Z-stack high-resolution confocal images showing staining for DPP4 in the reticular dermis and hair follicle niche of adult *Pdgfra*^{eGFP/+} knock-in mice. DP: dermal papilla (n=2). Scale bar, 20 μ m. (D) Outline of ventricle isolation, tissue dissociation, antibody staining and later flow cytometry from male *Pdgfra*^{eGFP/+} knock-in mice. (E) Representative flow cytometry and gating strategy of viable eGFP⁺ cardiac fibroblasts obtained from ventricles of male *Pdgfra*^{eGFP/+} knock-in mice. Debris was removed by size and doublets were excluded. Live cells were selected by the absence of DAPI staining (n=3).

Figure S15

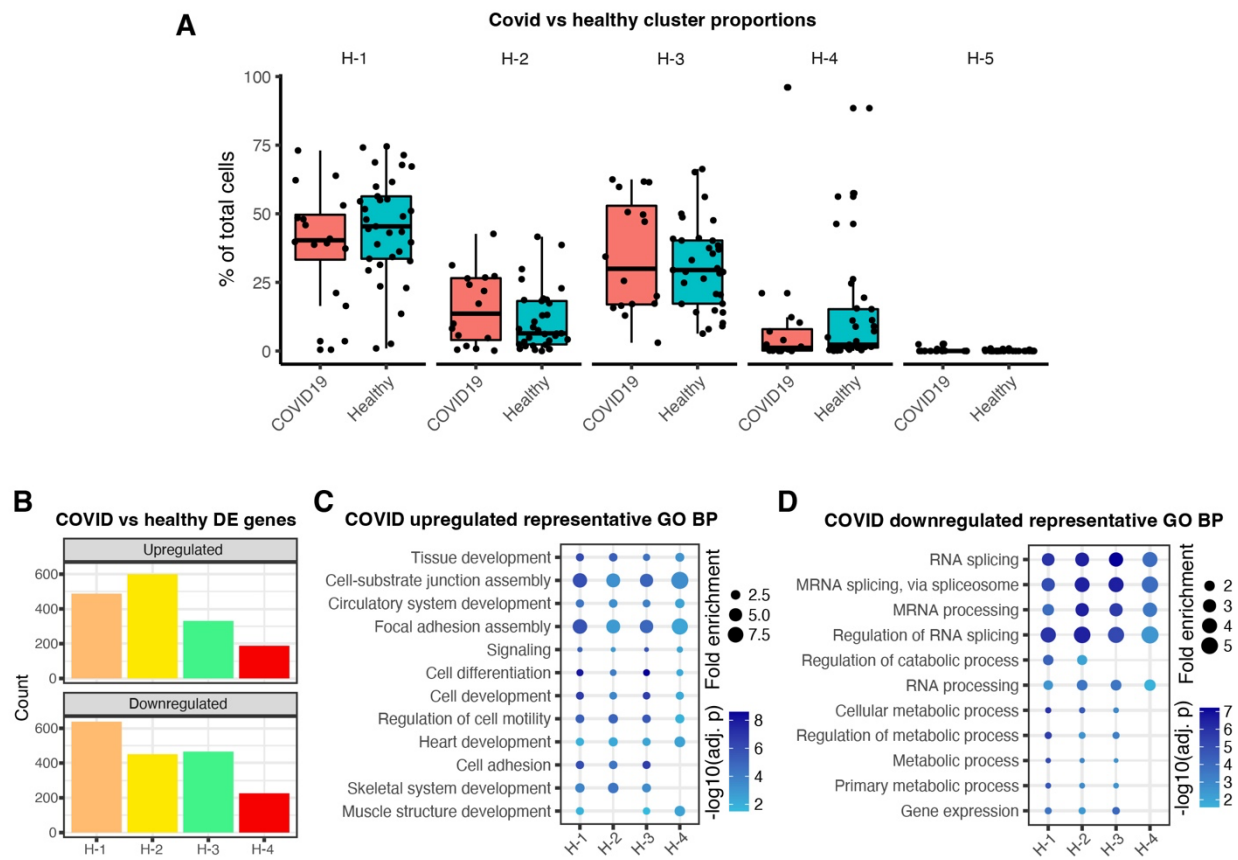


Fig. S15. Analysis of human CF subpopulation in COVID-19 infected versus control hearts. (A) Analysis of percentage of cells from uninfected or COVID-19 infected individuals predicted to correspond to the indicated human fibroblast cell type identified from healthy hearts in Sim and colleagues. (70). Shown are the percentage of cells per individual. (B) Counts of up- and downregulated DE genes between COVID and healthy cardiac fibroblasts. (C,D) Representative GO BP terms over-represented among (C) genes upregulated with COVID infection and (D) genes downregulated with COVID infection.

Figure S16

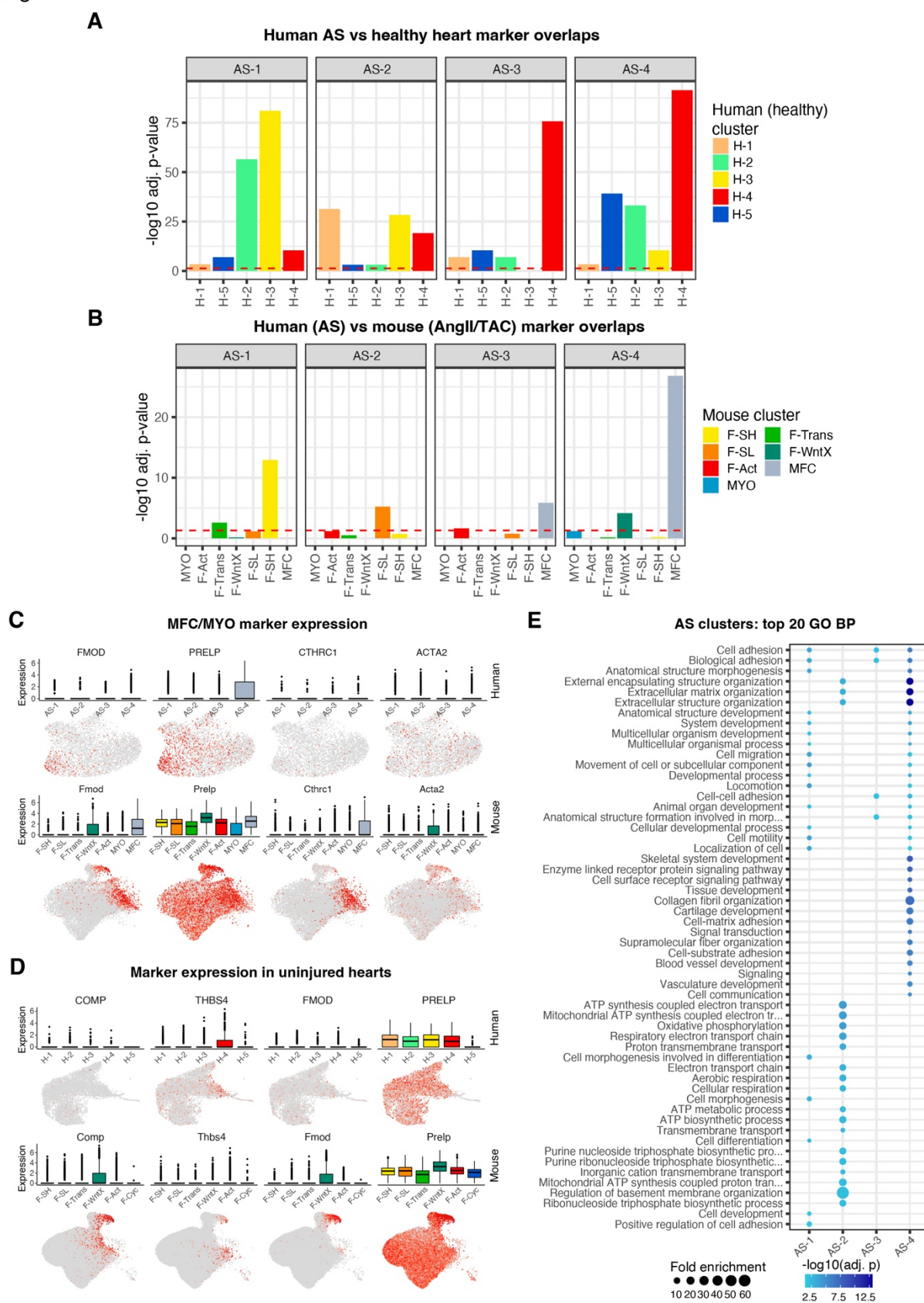


Fig. S16. Comparison of fibroblast states in diseased mouse and human hearts. (A) Overlap of marker genes (MAST testing; $p_{adj} < 1 \times 10^{-5}$; log2-fold change > 0.5) from the cardiac fibroblast clusters identified in healthy human hearts from Sim and colleagues (3) with fibroblast clusters from aortic stenosis (AS) hearts (22). Indicated are adjusted p -values from Fisher's exact tests. (B) As for (A) but comparing marker genes from murine cardiac fibroblasts from AngII or TAC hearts to human cardiac fibroblasts from AS hearts. (C) Expression of select MYO/MFC markers in (top) diseased human cardiac fibroblasts or (bottom) mouse fibroblasts from hearts of AngII or TAC affected animals. (D) Expression of select markers for MFC or F-WntX in (top) healthy human hearts or (bottom) uninjured mouse hearts. (E) Top 20 GO Biological Process terms overrepresented in marker genes for each of the four AS human cardiac fibroblast clusters.

Figure S17

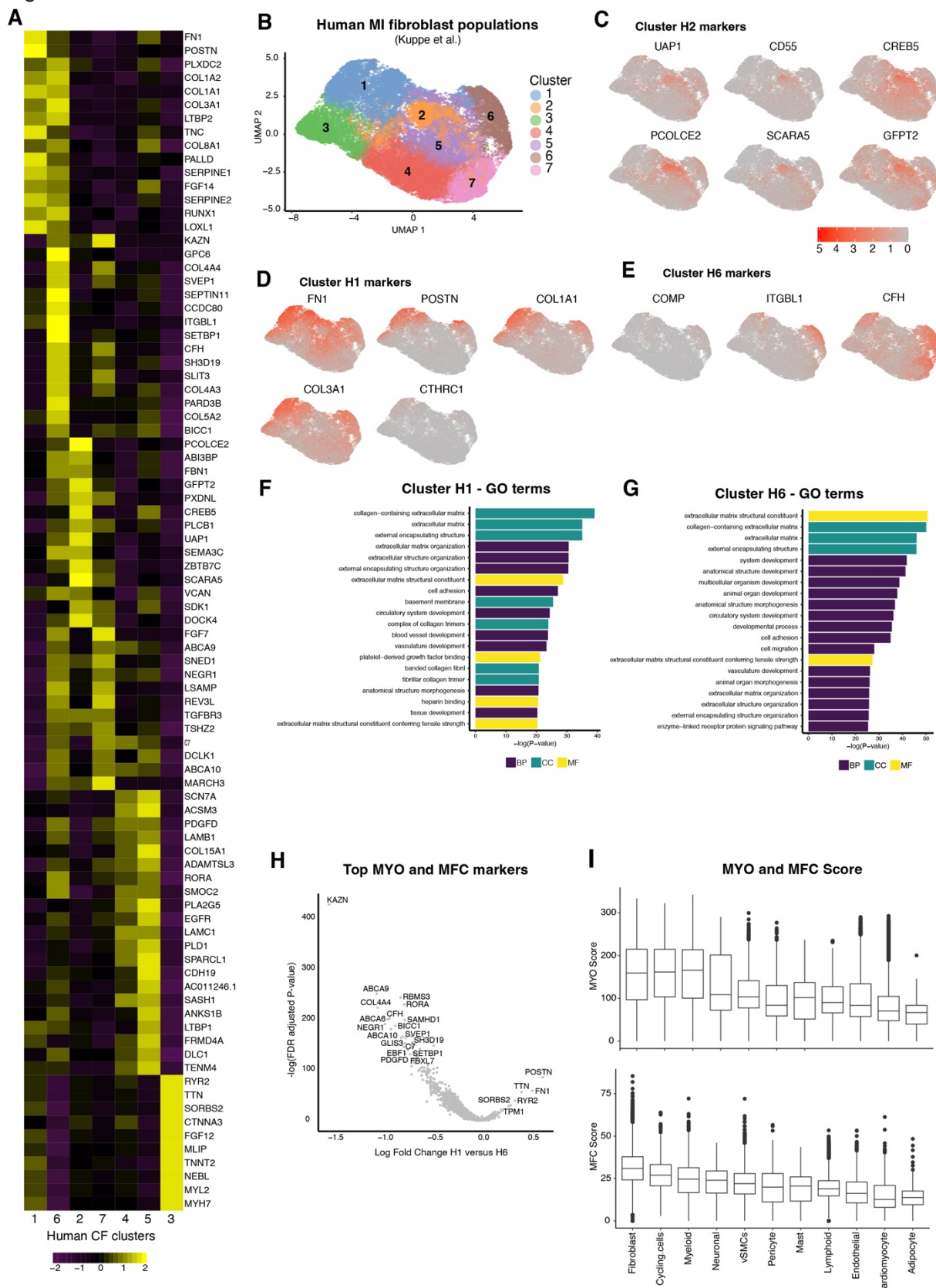
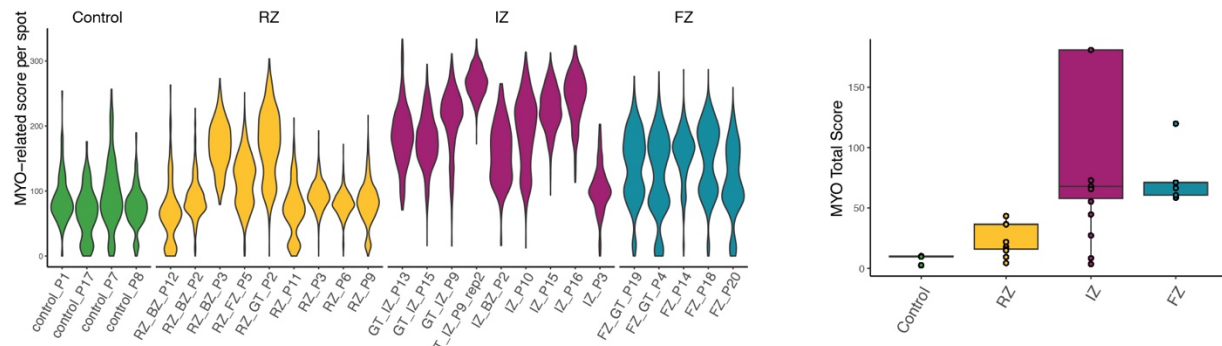


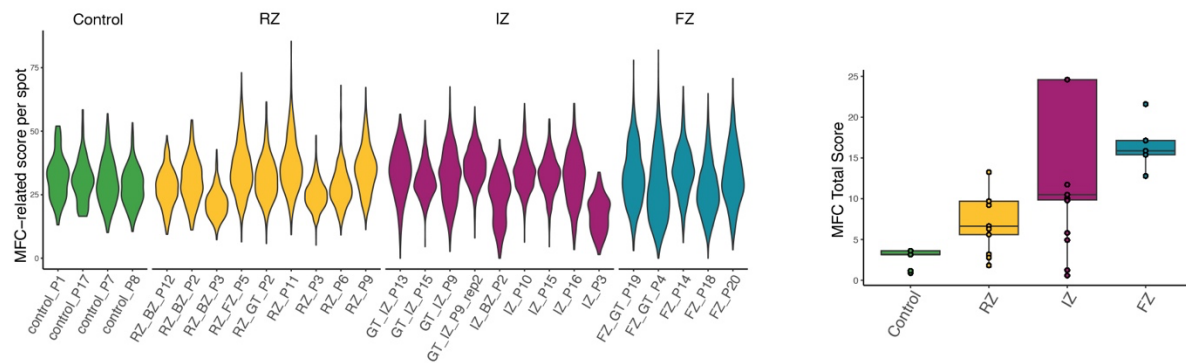
Fig. S17. Analysis of cardiac fibroblasts from human MI hearts. (A) Heatmap of gene expression of human MI fibroblast populations split by unbiased clusters. (B) UMAP of scRNA-seq-resolved human MI fibroblast populations coloured by unbiased clusters. (C) UMAP as in panel A displaying gene expression for selected marker genes for H2. (D) As in panel B for selected marker genes for H1. (E) As in panel B for selected marker genes for H6. (F) Barplot displaying -log(P-value) for the top significantly enriched gene ontology terms associated with cluster H1. (G) As in panel E for cluster H6. (H) Volcano plot displaying log fold change of cluster H1 versus H6 against -log(FDR adjusted P-value). Top genes are labelled on both sides. (I) Boxplots displaying MYO and MFC scores calculated for scRNA-seq-resolved human cells, split by the cell type label. Cell types are sorted according to decreasing mean score for MYO and MFC respectively.

Figure S18

A



B



C

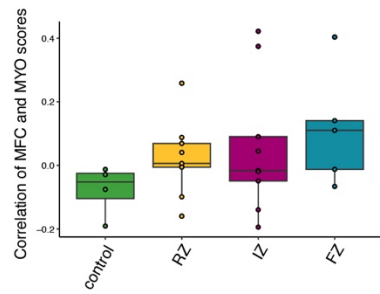


Fig. S18. MYO and MFC scores among clinical samples and heart anatomical regions. (A) Violin plots displaying MYO scores calculated over each Visium-resolved spot, split by patient sample and arranged according to sample type (left), and boxplots displaying total MYO score across entire Visium-resolved sample for each patient arranged by sample type (right). (B) As in panel A for MFC. (C) Boxplots indicating Pearson correlation of MYO and MFC scores for each Visium-resolved spot within each patient sample, arranged by sample type.

Figure S19

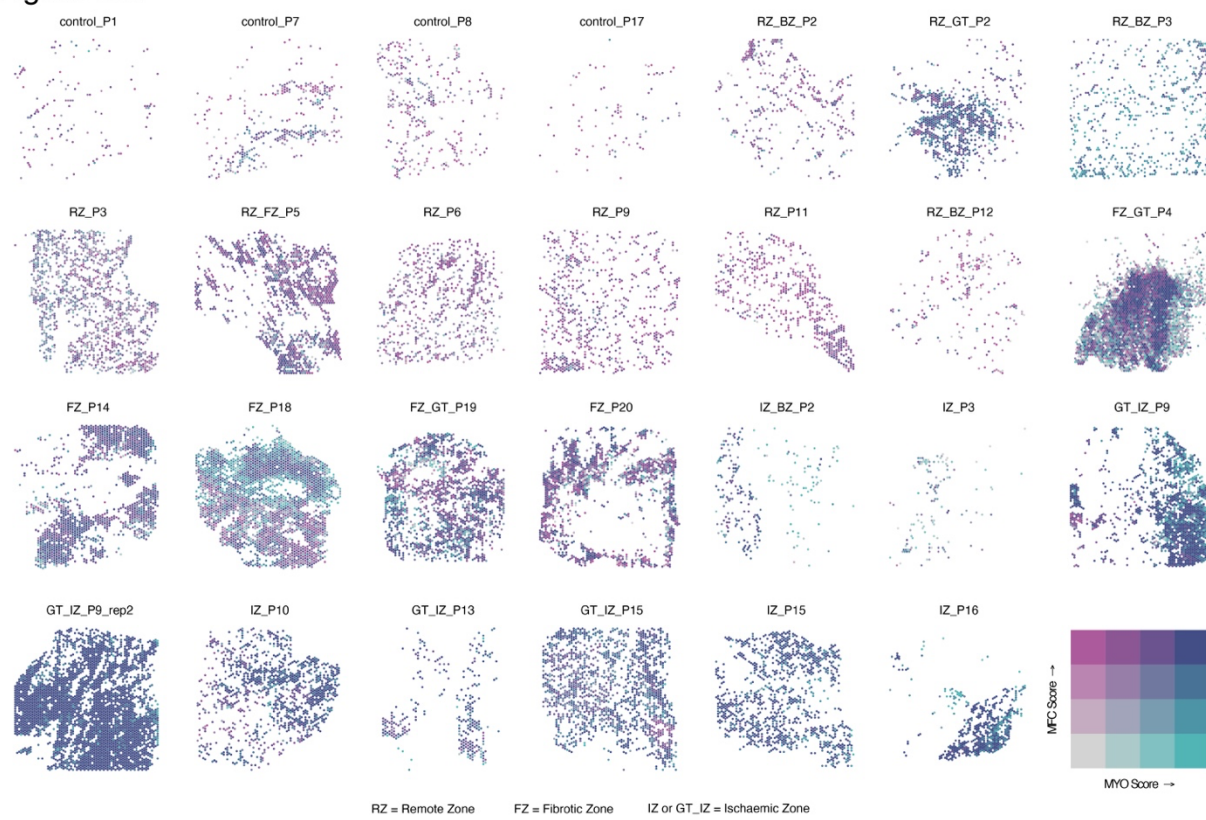


Fig. S19. MYO and MFC scores in clinical samples. Spatial coordinates of Visium-resolved spots in human MI samples, coloured using bivariate colour scheme corresponding to MFC and MYO scores. Only spots corresponding to majority Fibroblast percentage are displayed. Patient samples are arranged according to control, RZ, FZ, and IZ types by row from top to bottom.

Figure S20

Summary diagram: CF population dynamics in cardiac injury models

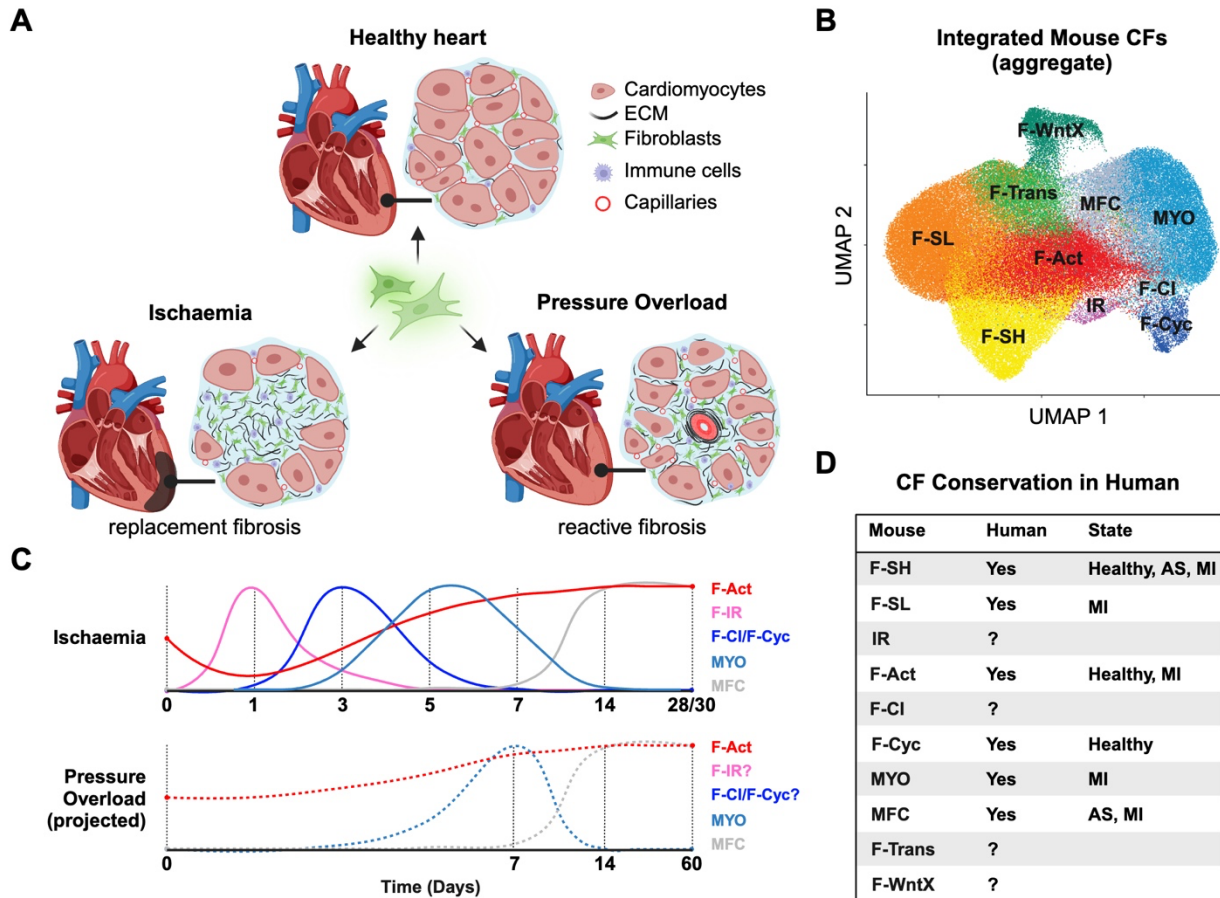


Figure S20. Summary diagram: CF population dynamics in cardiac injury models. (A) Schematic illustrating the two general categories of myocardial fibrosis - replacement fibrosis leading to scarring, as seen in MI and IRI, and reactive (interstitial and perivascular) fibrosis, as found in pressure overload. (B) UMAP plot showing an aggregate of integrated mouse CF data. (C) Projected CF population flux in ischemia versus pressure overload cardiac disease models. Note high homology between specific population involvement and their temporal dynamics. Dotted lines for pressure overload indicate that dynamics have been inferred from limited temporally resolved data. (D) Summary of evidence for conservation of mouse CF states in human hearts investigated in this study.

Supplemental auxiliary files:

Table S1. Differentially expressed genes in CF subsets.

Table S2. Differentially expressed genes between early CF subtypes.

Table S3. Differentially expressed genes within the MYO forming populations.

Table S4. Top 20 inferred transcription factor (TF) networks between identified populations in the integrated MI data.

Table S5. Differentially expressed genes between MYO and MFC and between MYO-1 and MYO-2.

Table S6. Differentially expressed genes between integrated cells from AngII/TAC and MI-days 5-7

Table S7. DE and DTU genes for MFC vs F-SH comparisons across MI-day 14, MI-days 28/30, AngII and TAC.

Table S8. DE and DTU genes for F-Act vs F-SH comparisons

Table S9. Differentially expressed genes and associated GO terms between HFpEF and normal chow mice at week 15 for fibroblast populations.

Table S10. Differentially expressed genes for human fibroblast clusters in healthy and AS hearts plus relative weights assigned to each gene for MYO and MFC identities for calculation of human MYO and MFC scores.

REFERENCES AND NOTES

1. A. Tanay, A. Regev, Scaling single-cell genomics from phenomenology to mechanism. *Nature* **541**, 331–338 (2017).
2. J. E. Rood, A. Maartens, A. Hupalowska, S. A. Teichmann, A. Regev, Impact of the human cell atlas on medicine. *Nat. Med.* **28**, 2486–2496 (2022).
3. J. Lim, V. Chin, K. Fairfax, C. Moutinho, D. Suan, H. Ji, J. E. Powell, Transitioning single-cell genomics into the clinic. *Nat. Rev. Genet.* **24**, 573–584 (2023).
4. N. G. Frangogiannis, Cardiac fibrosis. *Cardiovasc. Res.* **117**, 1450–1488 (2021).
5. J. J. H. Chong, V. Chandrakanthan, M. Xaymardan, N. S. Asli, J. Li, I. Ahmed, C. Heffernan, M. K. Menon, C. J. Scarlett, A. Rashidianfar, C. Biben, H. Zoellner, E. K. Colvin, J. E. Pimanda, A. V. Biankin, B. Zhou, W. T. Pu, O. W. J. Prall, R. P. Harvey, Adult cardiac-resident MSC-like stem cells with a proepicardial origin. *Cell Stem Cell* **9**, 527–540 (2011).
6. H. Soliman, B. Paylor, R. W. Scott, D. R. Lemos, C. K. Chang, M. Arostegui, M. Low, C. Lee, D. Fiore, P. Braghetta, V. Pospichalova, C. E. Barkauskas, V. Korinek, A. Rampazzo, K. MacLeod, T. M. Underhill, F. M. V. Rossi, Pathogenic potential of Hic1-expressing cardiac stromal progenitors. *Cell Stem Cell* **26**, 205–220.e8 (2020).
7. J. T. Kuwabara, A. Hara, S. Bhutada, G. S. Gojanovich, J. Chen, K. Hokutan, V. Shettigar, A. Y. Lee, L. P. DeAngelo, J. R. Heckl, J. R. Jahansooz, D. K. Tacdol, M. T. Ziolo, S. S. Apte, M. D. Tallquist, Consequences of PDGFR α^+ fibroblast reduction in adult murine hearts. *eLife* **11**, e69854 (2022).
8. V. Janbandhu, V. Tallapragada, R. Patrick, Y. Li, D. Abeygunawardena, D. T. Humphreys, E. M. M. A. Martin, A. O. Ward, O. Contreras, N. Farbeh, E. Yao, J. du, S. L. Dunwoodie, N. Bursac, R. P. Harvey, Hif-1a suppresses ROS-induced proliferation of cardiac fibroblasts following myocardial infarction. *Cell Stem Cell* **29**, 281–297.e12 (2022).

9. N. Farbeh, R. Patrick, A. Dorison, M. Xaymardan, V. Janbandhu, K. Wystub-Lis, J. W. K. Ho, R. E. Nordon, R. P. Harvey, Single-cell expression profiling reveals dynamic flux of cardiac stromal, vascular and immune cells in health and injury. *eLife* **8**, e43882 (2019).
10. E. Forte, D. A. Skelly, M. Chen, S. Daigle, K. A. Morelli, O. Hon, V. M. Philip, M. W. Costa, N. A. Rosenthal, M. B. Furtado, Dynamic interstitial cell response during myocardial infarction predicts resilience to rupture in genetically diverse mice. *Cell Rep.* **30**, 3149–3163.e6 (2020).
11. E. A. Rog-Zielinska, R. A. Norris, P. Kohl, R. Markwald, The living scar—Cardiac fibroblasts and the injured heart. *Trends Mol. Med.* **22**, 99–114 (2016).
12. M. D. Tallquist, J. D. Molkentin, Redefining the identity of cardiac fibroblasts. *Nat. Rev. Cardiol.* **14**, 484–491 (2017).
13. M. Pesce, G. N. Duda, G. Forte, H. Girao, A. Raya, P. Roca-Cusachs, J. P. G. Sluijter, C. Tschöpe, S. Van Linthout, Cardiac fibroblasts and mechanosensation in heart development, health and disease. *Nat. Rev. Cardiol.* **20**, 309–324 (2023).
14. H. E. Talbott, S. Mascharak, M. Griffin, D. C. Wan, M. T. Longaker, Wound healing, fibroblast heterogeneity, and fibrosis. *Cell Stem Cell* **29**, 1161–1180 (2022).
15. R. Schuster, J. S. Rockel, M. Kapoor, B. Hinz, The inflammatory speech of fibroblasts. *Immunol. Rev.* **302**, 126–146 (2021).
16. A. González, E. B. Schelbert, J. Diez, J. Butler, Myocardial interstitial fibrosis in heart failure: Biological and translational perspectives. *J. Am. Coll. Cardiol.* **71**, 1696–1706 (2018).
17. M. Walraven, B. Hinz, Therapeutic approaches to control tissue repair and fibrosis: Extracellular matrix as a game changer. *Matrix Biol.* **71-72**, 205–224 (2018).
18. E. Forte, M. Ramialison, H. T. Nim, M. Mara, J. Y. Li, R. Cohn, S. L. Daigle, S. Boyd, E. G. Stanley, A. G. Elefanty, J. T. Hinson, M. W. Costa, N. A. Rosenthal, M. B. Furtado, Adult mouse fibroblasts retain organ-specific transcriptomic identity. *eLife* **11**, e71008 (2022).

19. M. Litviňuková, C. Talavera-López, H. Maatz, D. Reichart, C. L. Worth, E. L. Lindberg, M. Kanda, K. Polanski, M. Heinig, M. Lee, E. R. Nadelmann, K. Roberts, L. Tuck, E. S. Fasouli, D. M. De Laughter, B. M. Donough, H. Wakimoto, J. M. Gorham, S. Samari, K. T. Mahbubani, K. Saeb-Parsy, G. Patone, J. J. Boyle, H. Zhang, H. Zhang, A. Viveiros, G. Y. Oudit, O. A. Bayraktar, J G Seidman, C. E. Seidman, M. Noseda, N. Hubner, S. A. Teichmann, Cells of the adult human heart. *Nature* **588**, 466–472 (2020).
20. M. Chaffin, I. Papangeli, B. Simonson, A. D. Akkad, M. C. Hill, A. Arduini, S. J. Fleming, M. Melanson, S. Hayat, M. Kost-Alimova, O. Atwa, J. Ye, K. C. Bedi Jr., M. Nahrendorf, V. K. Kaushik, C. M. Stegmann, K. B. Margulies, N. R. Tucker, P. T. Ellinor, Single-nucleus profiling of human dilated and hypertrophic cardiomyopathy. *Nature* **608**, 174–180 (2022).
21. C. Kuppe, R. O. Ramirez Flores, Z. Li, S. Hayat, R. T. Levinson, X. Liao, M. T. Hannani, J. Tanevski, F. Wünnemann, J. S. Nagai, M. Halder, D. Schumacher, S. Menzel, G. Schäfer, K. Hoeft, M. Cheng, S. Ziegler, X. Zhang, F. Peisker, N. Kaesler, T. Saritas, Y. Xu, A. Kassner, J. Gummert, M. Morshuis, J. Amrute, R. J. A. Veltrop, P. Boor, K. Klingel, L. W. van Laake, A. Vink, R. M. Hoogenboezem, E. M. J. Bindels, L. Schurgers, S. Sattler, D. Schapiro, R. K. Schneider, K. Lavine, H. Milting, I. G. Costa, J. Saez-Rodriguez, R. Kramann, Spatial multi-omic map of human myocardial infarction. *Nature* **608**, 766–777 (2022).
22. L. Nicin, S. M. Schroeter, S. F. Glaser, R. Schulze-Brünning, M. D. Pham, S. S. Hille, M. Yekelchyk, B. Kattih, W. T. Abplanalp, L. Tombor, O. J. Müller, T. Braun, B. Meder, C. Reich, M. Arsalan, T. Holubec, T. Walther, F. Emrich, J. Krishnan, A. M. Zeiher, D. John, S. Dimmeler, A human cell atlas of the pressure-induced hypertrophic heart. *Nat. Cardiovasc. Res.* **1**, 174–185 (2022).
23. W. T. Abplanalp, N. Tucker, S. Dimmeler, Single-cell technologies to decipher cardiovascular diseases. *Eur. Heart J.* **43**, 4536–4547 (2022).
24. A. M. A. Miranda, V. Janbandhu, H. Maatz, K. Kanemaru, J. Cranley, S. A. Teichmann, N. Hübner, M. D. Schneider, R. P. Harvey, M. Noseda, Single-cell transcriptomics for the assessment of cardiac disease. *Nat. Rev. Cardiol.* **20**, 289–308 (2023).

25. M. Peng, Y. Li, B. Wamsley, Y. Wei, K. Roeder, Integration and transfer learning of single-cell transcriptomes via cFIT. *Proc. Natl. Acad. Sci. U.S.A.* **118**, e2024383118 (2021).
26. T. Stuart, A. Butler, P. Hoffman, C. Hafemeister, E. Papalexi, W. M. Mauck III, Y. Hao, M. Stoeckius, P. Smibert, R. Satija, Comprehensive integration of single-cell data. *Cell* **177**, 1888–1902.e21 (2019).
27. J. F. Ouyang, U. S. Kamaraj, E. Y. Cao, O. J. L. Rackham, ShinyCell: Simple and sharable visualization of single-cell gene expression data. *Bioinformatics* **37**, 3374–3376 (2021).
28. A. Ruiz-Villalba, J. P. Romero, S. C. Hernández, A. Vilas-Zornoza, N. Fortelny, L. Castro-Labrador, P. San Martin-Uriz, E. Lorenzo-Vivas, P. García-Oolloqui, M. Palacio, J. J. Gavira, G. Bastarrika, S. Janssens, M. Wu, E. Iglesias, G. Abizanda, X. M. de Morentin, M. Lasaga, N. Planell, C. Bock, D. Alignani, G. Medal, I. Prudovsky, Y. R. Jin, S. Ryzhov, H. Yin, B. Pelacho, D. Gomez-Cabrero, V. Lindner, D. Lara-Astiaso, F. Prósper, Single-cell RNA sequencing analysis reveals a crucial role for CTHRC1 (collagen triple helix repeat containing 1) cardiac fibroblasts after myocardial infarction. *Circulation* **142**, 1831–1847 (2020).
29. I. Korsunsky, N. Millard, J. Fan, K. Slowikowski, F. Zhang, K. Wei, Y. Baglaenko, M. Brenner, P. R. Loh, S. Raychaudhuri, Fast, sensitive and accurate integration of single-cell data with Harmony. *Nat. Methods* **16**, 1289–1296 (2019).
30. Y. Liu, T. Wang, B. Zhou, D. Zheng, Robust integration of multiple single-cell RNA sequencing datasets using a single reference space. *Nat. Biotechnol.* **39**, 877–884 (2021).
31. M. Noseda, M. Harada, S. McSweeney, T. Leja, E. Belian, D. J. Stuckey, M. S. Abreu Paiva, J. Habib, I. Macaulay, A. J. de Smith, F. al-Beidh, R. Sampson, R. T. Lumbers, P. Rao, S. E. Harding, A. I. F. Blakemore, S. Eirik Jacobsen, M. Barahona, M. D. Schneider, PDGFR α demarcates the cardiogenic clonogenic Sca1 $^+$ stem/progenitor cell in adult murine myocardium. *Nat. Commun.* **6**, 6930 (2015).
32. R. Kramann, R. K. Schneider, D. P. DiRocco, F. Machado, S. Fleig, P. A. Bondzie, J. M. Henderson, B. L. Ebert, B. D. Humphreys, Perivascular Gli1 $^+$ progenitors are key contributors to injury-induced organ fibrosis. *Cell Stem Cell* **16**, 51–66 (2015).

33. Y. Kfouri, D. T. Scadden, Mesenchymal cell contributions to the stem cell niche. *Cell Stem Cell* **16**, 239–253 (2015).
34. P. Cattaneo, D. Mukherjee, S. Spinozzi, L. Zhang, V. Larcher, W. B. Stallcup, H. Kataoka, J. Chen, S. Dimmeler, S. M. Evans, N. Guimarães-Camboa, Parallel lineage-tracing studies establish fibroblasts as the prevailing *in vivo* adipocyte progenitor. *Cell Rep.* **30**, 571–582.e2 (2020).
35. O. Contreras, F. M. V. Rossi, M. Theret, Origins, potency, and heterogeneity of skeletal muscle fibro-adipogenic progenitors-time for new definitions. *Skelet. Muscle* **11**, 16 (2021).
36. C. K. F. Chan, P. Lindau, W. Jiang, J. Y. Chen, L. F. Zhang, C.-C. Chen, J. Seita, D. Sahoo, J.-B. Kim, A. Lee, S. Park, D. Nag, Y. Gong, S. Kulkarni, C. A. Luppen, A. A. Theologis, D. C. Wan, A. De Boer, E. Y. Seo, J. D. Vincent-Tompkins, K. Loh, G. G. Walmsley, D. L. Kraft, J. C. Wu, M. T. Longaker, I. L. Weissman, Clonal precursor of bone, cartilage, and hematopoietic niche stromal cells. *Proc. Natl. Acad. Sci. U.S.A.* **110**, 12643–12648 (2013).
37. D. L. Worthley, M. Churchill, J. T. Compton, Y. Tailor, M. Rao, Y. Si, D. Levin, M. G. Schwartz, A. Uygur, Y. Hayakawa, S. Gross, B. W. Renz, W. Setlik, A. N. Martinez, X. Chen, S. Nizami, H. G. Lee, H. P. Kang, J. M. Caldwell, S. Asfaha, C. B. Westphalen, T. Graham, G. Jin, K. Nagar, H. Wang, M. A. Kheirbek, A. Kolhe, J. Carpenter, M. Glaire, A. Nair, S. Renders, N. Manieri, S. Muthupalani, J. G. Fox, M. Reichert, A. S. Giraud, R. F. Schwabe, J. P. Pradere, K. Walton, A. Prakash, D. Gumucio, A. K. Rustgi, T. S. Stappenbeck, R. A. Friedman, M. D. Gershon, P. Sims, T. Grikscheit, F. Y. Lee, G. Karsenty, S. Mukherjee, T. C. Wang, Gremlin 1 identifies a skeletal stem cell with bone, cartilage, and reticular stromal potential. *Cell* **160**, 269–284 (2015).
38. I. C. L. Pillai, S. Li, M. Romay, L. Lam, Y. Lu, J. Huang, N. Dillard, M. Zemanova, L. Rubbi, Y. Wang, J. Lee, M. Xia, O. Liang, Y. H. Xie, M. Pellegrini, A. J. Lusis, A. Deb, Cardiac fibroblasts adopt osteogenic fates and can be targeted to attenuate pathological heart calcification. *Cell Stem Cell* **20**, 218–232.e5 (2017).
39. A. Kohela, E. van Rooij, Fibro-fatty remodelling in arrhythmogenic cardiomyopathy. *Basic Res. Cardiol.* **117**, 22 (2022).

40. L. Muhl, G. Genové, S. Leptidis, J. Liu, L. He, G. Mocci, Y. Sun, S. Gustafsson, B. Buyandelger, I. V. Chivukula, Å. Segerstolpe, E. Raschperger, E. M. Hansson, J. L. M. Björkegren, X. R. Peng, M. Vanlandewijck, U. Lendahl, C. Betsholtz, Single-cell analysis uncovers fibroblast heterogeneity and criteria for fibroblast and mural cell identification and discrimination. *Nat. Commun.* **11**, 3953 (2020).
41. M. Nahrendorf, F. K. Swirski, E. Aikawa, L. Stangenberg, T. Wurdinger, J. L. Figueiredo, P. Libby, R. Weissleder, M. J. Pittet, The healing myocardium sequentially mobilizes two monocyte subsets with divergent and complementary functions. *J. Exp. Med.* **204**, 3037–3047 (2007).
42. G. D. Duerr, D. Dewald, E. J. Schmitz, L. Verfuerth, K. Keppel, C. Peigney, A. Ghanem, A. Welz, O. Dewald, Metallothioneins 1 and 2 modulate inflammation and support remodeling in ischemic cardiomyopathy in mice. *Mediators Inflamm.* **2016**, 7174127 (2016).
43. H. Abe, Y. Tanada, S. Omiya, M. N. Podaru, T. Murakawa, J. Ito, A. M. Shah, S. J. Conway, M. Ono, K. Otsu, NF- κ B activation in cardiac fibroblasts results in the recruitment of inflammatory Ly6C^{hi} monocytes in pressure-overloaded hearts. *Sci. Signal.* **14**, eabe4932 (2021).
44. R. Patrick, D. T. Humphreys, V. Janbandhu, A. Oshlack, J. W. K. Ho, R. P. Harvey, K. K. Lo, Sierra: Discovery of differential transcript usage from polyA-captured single-cell RNA-seq data. *Genome Biol.* **21**, 167 (2020).
45. R. Sandberg, J. R. Neilson, A. Sarma, P. A. Sharp, C. B. Burge, Proliferating cells express mRNAs with shortened 3' untranslated regions and fewer microRNA target sites. *Science* **320**, 1643–1647 (2008).
46. X. Fu, H. Khalil, O. Kanisicak, J. G. Boyer, R. J. Vagnozzi, B. D. Maliken, M. A. Sargent, V. Prasad, I. Valiente-Alandi, B. C. Blaxall, J. D. Molkentin, Specialized fibroblast differentiated states underlie scar formation in the infarcted mouse heart. *J. Clin. Invest.* **128**, 2127–2143 (2018).
47. F. Peisker, M. Halder, J. Nagai, S. Ziegler, N. Kaesler, K. Hoeft, R. Li, E. M. J. Bindels, C. Kuppe, J. Moellmann, M. Lehrke, C. Stoppe, M. T. Schaub, R. K. Schneider, I. Costa, R. Kramann, Mapping the cardiac vascular niche in heart failure. *Nat. Commun.* **13**, 3027 (2022).

48. F. A. Wolf, F. K. Hamey, M. Plass, J. Solana, J. S. Dahlin, B. Göttgens, N. Rajewsky, L. Simon, F. J. Theis, PAGA: Graph abstraction reconciles clustering with trajectory inference through a topology preserving map of single cells. *Genome Biol.* **20**, 59 (2019).
49. J. Cao, M. Spielmann, X. Qiu, X. Huang, D. M. Ibrahim, A. J. Hill, F. Zhang, S. Mundlos, L. Christiansen, F. J. Steemers, C. Trapnell, J. Shendure, The single-cell transcriptional landscape of mammalian organogenesis. *Nature* **566**, 496–502 (2019).
50. G. Finak, A. McDavid, M. Yajima, J. Deng, V. Gersuk, A. K. Shalek, C. K. Slichter, H. W. Miller, M. J. McElrath, M. Prlic, P. S. Linsley, R. Gottardo, MAST: A flexible statistical framework for assessing transcriptional changes and characterizing heterogeneity in single-cell RNA sequencing data. *Genome Biol.* **16**, 278 (2015).
51. M. Alexanian, P. F. Przytycki, R. Micheletti, A. Padmanabhan, L. Ye, J. G. Travers, B. Gonzalez-Teran, A. C. Silva, Q. Duan, S. S. Ranade, F. Felix, R. Linares-Saldana, L. Li, C. Y. Lee, N. Sadagopan, A. Pelonero, Y. Huang, G. Andreoletti, R. Jain, T. A. McKinsey, M. G. Rosenfeld, C. A. Gifford, K. S. Pollard, S. M. Haldar, D. Srivastava, A transcriptional switch governs fibroblast activation in heart disease. *Nature* **595**, 438–443 (2021).
52. P. L. Roche, R. S. Nagalingam, R. A. Bagchi, N. Aroutiounova, B. M. J. Belisle, J. T. Wigle, M. P. Czubryt, Role of scleraxis in mechanical stretch-mediated regulation of cardiac myofibroblast phenotype. *Am. J. Physiol. Cell Physiol.* **311**, C297–C307 (2016).
53. P. Badia-I-Mompel, J. V. Santiago, J. Braunger, C. Geiss, D. Dimitrov, S. Müller-Dott, P. Taus, A. Dugourd, C. H. Holland, R. O. R. Flores, J. Saez-Rodriguez, decoupleR: Ensemble of computational methods to infer biological activities from omics data. *Bioinform. Adv.* **2**, vbac016 (2022).
54. W. Ni, A. A. Perez, S. Schreiner, C. M. Nicolet, P. J. Farnham, Characterization of the ZFX family of transcription factors that bind downstream of the start site of CpG island promoters. *Nucleic Acids Res.* **48**, 5986–6000 (2020).
55. X. Chen, H. Xu, P. Yuan, F. Fang, M. Huss, V. B. Vega, E. Wong, Y. L. Orlov, W. Zhang, J. Jiang, Y. H. Loh, H. C. Yeo, Z. X. Yeo, V. Narang, K. R. Govindarajan, B. Leong, A. Shahab, Y. Ruan, G.

- Bourque, W. K. Sung, N. D. Clarke, C. L. Wei, H. H. Ng, Integration of external signaling pathways with the core transcriptional network in embryonic stem cells. *Cell* **133**, 1106–1117 (2008).
56. A. Chaves-Sanjuan, N. Gnesutta, A. Gobbini, D. Martignago, A. Bernardini, F. Fornara, R. Mantovani, M. Nardini, Structural determinants for NF-Y subunit organization and NF-Y/DNA association in plants. *Plant J.* **105**, 49–61 (2021).
57. D. Dolfini, R. Gatta, R. Mantovani, NF-Y and the transcriptional activation of CCAAT promoters. *Crit. Rev. Biochem. Mol. Biol.* **47**, 29–49 (2012).
58. N. Ding, R. T. Yu, N. Subramaniam, M. H. Sherman, C. Wilson, R. Rao, M. Leblanc, S. Coulter, M. He, C. Scott, S. L. Lau, A. R. Atkins, G. D. Barish, J. E. Gunton, C. Liddle, M. Downes, R. M. Evans, A vitamin D receptor/SMAD genomic circuit gates hepatic fibrotic response. *Cell* **153**, 601–613 (2013).
59. D. Palioura, A. Lazou, K. Drosatos, Krüppel-like factor (KLF)5: An emerging foe of cardiovascular health. *J. Mol. Cell. Cardiol.* **163**, 56–66 (2022).
60. Q. Zhang, L. Wang, S. Wang, H. Cheng, L. Xu, G. Pei, Y. Wang, C. Fu, Y. Jiang, C. He, Q. Wei, Signaling pathways and targeted therapy for myocardial infarction. *Signal. Transduct. Target. Ther.* **7**, 78 (2022).
61. L. Aryan, D. Younessi, M. Zargari, S. Banerjee, J. Agopian, S. Rahman, R. Borna, G. Ruffenach, S. Umar, M. Eghbali, The role of estrogen receptors in cardiovascular disease. *Int. J. Mol. Sci.* **21**, 4314 (2020).
62. J. Hesse, C. Owenier, T. Lautwein, R. Zalfen, J. F. Weber, Z. Ding, C. Alter, A. Lang, M. Grandoch, N. Gerdes, J. W. Fischer, G. W. Klau, C. Dieterich, K. Köhrer, J. Schrader, Single-cell transcriptomics defines heterogeneity of epicardial cells and fibroblasts within the infarcted murine heart. *eLife* **10**, e65921 (2021).
63. M. A. McLellan, D. A. Skelly, M. S. I. Dona, G. T. Squiers, G. E. Farrugia, T. L. Gaynor, C. D. Cohen, R. Pandey, H. Diep, A. Vinh, N. A. Rosenthal, A. R. Pinto, High-resolution transcriptomic profiling of the heart during chronic stress reveals cellular drivers of cardiac fibrosis and hypertrophy. *Circulation* **142**, 1448–1463 (2020).

64. O. Stenina-Adognravi, E. F. Plow, Thrombospondin-4 in tissue remodeling. *Matrix Biol.* **75-76**, 300–313 (2019).
65. C. L. Zhang, Q. Zhao, H. Liang, X. Qiao, J. Y. Wang, D. Wu, L. L. Wu, L. Li, Cartilage intermediate layer protein-1 alleviates pressure overload-induced cardiac fibrosis via interfering TGF- β 1 signaling. *J. Mol. Cell. Cardiol.* **116**, 135–144 (2018).
66. K. Schimmel, K. Ichimura, S. Reddy, F. Haddad, E. Spiekerkoetter, Cardiac fibrosis in the pressure overloaded left and right ventricle as a therapeutic target. *Front. Cardiovasc. Med.* **9**, 886553 (2022).
67. S. R. Ali, S. Ranjbarvaziri, M. Talkhabi, P. Zhao, A. Subat, A. Hojjat, P. Kamran, A. M. S. Müller, K. S. Volz, Z. Tang, K. Red-Horse, R. Ardehali, Developmental heterogeneity of cardiac fibroblasts does not predict pathological proliferation and activation. *Circ. Res.* **115**, 625–635 (2014).
68. H. Khalil, O. Kanisicak, V. Prasad, R. N. Correll, X. Fu, T. Schips, R. J. Vagnozzi, R. Liu, T. Huynh, S. J. Lee, J. Karch, J. D. Molkentin, Fibroblast-specific TGF- β –Smad2/3 signaling underlies cardiac fibrosis. *J. Clin. Invest.* **127**, 3770–3783 (2017).
69. T. Moore-Morris, N. Guimarães-Camboa, I. Banerjee, A. C. Zambon, T. Kisseleva, A. Velayoudon, W. B. Stallcup, Y. Gu, N. D. Dalton, M. Cedenilla, R. Gomez-Amaro, B. Zhou, D. A. Brenner, K. L. Peterson, J. Chen, S. M. Evans, Resident fibroblast lineages mediate pressure overload-induced cardiac fibrosis. *J. Clin. Invest.* **124**, 2921–2934 (2014).
70. R. S. Nagalingam, S. Chattopadhyaya, D. S. al-Hattab, D. Y. C. Cheung, L. Y. Schwartz, S. Jana, N. Aroutiounova, D. A. Ledingham, T. L. Moffatt, N. M. Landry, R. A. Bagchi, I. M. C. Dixon, J. T. Wigle, G. Y. Oudit, Z. Kassiri, D. S. Jassal, M. P. Czubryt, Scleraxis and fibrosis in the pressure-overloaded heart. *Eur. Heart J.* **43**, 4739–4750 (2022).
71. N. Ngwenyama, K. Kaur, D. Bugg, B. Theall, M. Aronovitz, R. Berland, S. Panagiotidou, C. Genco, M. A. Perrin, J. Davis, P. Alcaide, Antigen presentation by cardiac fibroblasts promotes cardiac dysfunction. *Nat. Cardiovasc. Res.* **1**, 761–774 (2022).

72. L. Alex, I. Russo, V. Holoborodko, N. G. Frangogiannis, Characterization of a mouse model of obesity-related fibrotic cardiomyopathy that recapitulates features of human heart failure with preserved ejection fraction. *Am. J. Physiol. Heart Circ. Physiol.* **315**, H934–H949 (2018).
73. D. Mahajan, S. Kancharla, P. Kolli, A. K. Sharma, S. Singh, S. Kumar, A. K. Mohanty, M. K. Jena, Role of fibulins in embryonic stage development and their involvement in various diseases. *Biomolecules* **11**, 685 (2021).
74. T. Sagae, M. Yokogawa, R. Sawazaki, Y. Ishii, N. Hosoda, S. I. Hoshino, S. Imai, I. Shimada, M. Osawa, Paip2A inhibits translation by competitively binding to the RNA recognition motifs of PABPC1 and promoting its dissociation from the poly(A) tail. *J. Biol. Chem.* **298**, 101844 (2022).
75. S. Chorghade, J. Seimetz, R. Emmons, J. Yang, S. M. Bresson, M. D. Lisio, G. Parise, N. K. Conrad, A. Kalsotra, Poly(A) tail length regulates PABPC1 expression to tune translation in the heart. *eLife* **6**, e24139 (2017).
76. L. S. Kilian, J. Voran, D. Frank, A. Y. Rangrez, RhoA: A dubious molecule in cardiac pathophysiology. *J. Biomed. Sci.* **28**, 33 (2021).
77. J. Roh, J. A. Hill, A. Singh, M. Valero-Munoz, F. Sam, Heart failure with preserved ejection fraction: Heterogeneous syndrome, diverse preclinical models. *Circ. Res.* **130**, 1906–1925 (2022).
78. G. G. Schiattarella, F. Altamirano, D. Tong, K. M. French, E. Villalobos, S. Y. Kim, X. Luo, N. Jiang, H. I. May, Z. V. Wang, T. M. Hill, P. P. A. Mammen, J. Huang, D. I. Lee, V. S. Hahn, K. Sharma, D. A. Kass, S. Lavandero, T. G. Gillette, J. A. Hill, Nitrosative stress drives heart failure with preserved ejection fraction. *Nature* **568**, 351–356 (2019).
79. G. G. Schiattarella, F. Altamirano, S. Y. Kim, D. Tong, A. Ferdous, H. Pirstine, S. Dasgupta, X. Wang, K. M. French, E. Villalobos, S. B. Spurgin, M. Waldman, N. Jiang, H. I. May, T. M. Hill, Y. Luo, H. Yoo, V. G. Zaha, S. Lavandero, T. G. Gillette, J. A. Hill, Xbp1s-FoxO1 axis governs lipid accumulation and contractile performance in heart failure with preserved ejection fraction. *Nat. Commun.* **12**, 1684 (2021).

80. C. B. Sim, B. Phipson, M. Ziemann, H. Rafehi, R. J. Mills, K. I. Watt, K. D. Abu-Bonsrah, R. K. R. Kalathur, H. K. Voges, D. T. Dinh, M. ter Huurne, C. J. Vivien, A. Kaspi, H. Kaipananickal, A. Hidalgo, L. M. D. Delbridge, R. L. Robker, P. Gregorevic, C. G. dos Remedios, S. Lal, A. T. Piers, I. E. Konstantinov, D. A. Elliott, A. el-Osta, A. Oshlack, J. E. Hudson, E. R. Porrello, Sex-specific control of human heart maturation by the progesterone receptor. *Circulation* **143**, 1614–1628 (2021).
81. L. Wang, Y. Yang, H. Ma, Y. Xie, J. Xu, D. Near, H. Wang, T. Garbutt, Y. Li, J. Liu, L. Qian, Single cell dual-omics reveals the transcriptomic and epigenomic diversity of cardiac non-myocytes. *Cardiovasc. Res.* **118**, 1548–1563 (2022).
82. M. B. Buechler, R. N. Pradhan, A. T. Krishnamurty, C. Cox, A. K. Calviello, A. W. Wang, Y. A. Yang, L. Tam, R. Caothien, M. Roose-Girma, Z. Modrusan, J. R. Arron, R. Bourgon, S. Müller, S. J. Turley, Cross-tissue organization of the fibroblast lineage. *Nature* **593**, 575–579 (2021).
83. D. Merrick, A. Sakers, Z. Irgebay, C. Okada, C. Calvert, M. P. Morley, I. Percec, P. Seale, Identification of a mesenchymal progenitor cell hierarchy in adipose tissue. *Science* **364**, eaav2501 (2019).
84. R. R. Driskell, F. M. Watt, Understanding fibroblast heterogeneity in the skin. *Trends Cell Biol.* **25**, 92–99 (2015).
85. W. Haussner, A. P. DeRosa, D. Haussner, J. Tran, J. Torres-Lavoro, J. Kamler, K. Shah, COVID-19 associated myocarditis: A systematic review. *Am. J. Emerg. Med.* **51**, 150–155 (2022).
86. M. I. Brener, M. L. Hulke, N. Fukuma, S. Golob, R. S. Zilinyi, Z. Zhou, C. Tzimas, I. Russo, C. McGroder, R. D. Pfeiffer, A. Chong, G. Zhang, D. Burkhoff, M. B. Leon, M. S. Maurer, J. W. Moses, A. C. Uhlemann, H. Hibshoosh, N. Uriel, M. J. Szabolcs, B. Redfors, C. C. Marboe, M. R. Baldwin, N. R. Tucker, E. J. Tsai, Clinico-histopathologic and single-nuclei RNA-sequencing insights into cardiac injury and microthrombi in critical COVID-19. *JCI Insight* **7**, e154633 (2022).
87. X. Zou, K. Chen, J. Zou, P. Han, J. Hao, Z. Han, Single-cell RNA-seq data analysis on the receptor ACE2 expression reveals the potential risk of different human organs vulnerable to 2019-nCoV infection. *Front. Med.* **14**, 185–192 (2020).

88. T. M. Delorey, C. G. K. Ziegler, G. Heimberg, R. Normand, Y. Yang, Å. Segerstolpe, D. Abbondanza, S. J. Fleming, A. Subramanian, D. T. Montoro, K. A. Jagadeesh, K. K. Dey, P. Sen, M. Slyper, Y. H. Pita-Juárez, D. Phillips, J. Biermann, Z. Bloom-Ackermann, N. Barkas, A. Ganna, J. Gomez, J. C. Melms, I. Katsyv, E. Normandin, P. Naderi, Y. V. Popov, S. S. Raju, S. Niezen, L. T. Y. Tsai, K. J. Siddle, M. Sud, V. M. Tran, S. K. Vellarikkal, Y. Wang, L. Amir-Zilberstein, D. S. Atri, J. Beechem, O. R. Brook, J. Chen, P. Divakar, P. Dorceus, J. M. Engreitz, A. Essene, D. M. Fitzgerald, R. Fropf, S. Gazal, J. Gould, J. Grzyb, T. Harvey, J. Hecht, T. Hether, J. Jané-Valbuena, M. Leney-Greene, H. Ma, C. McCabe, D. E. McLoughlin, E. M. Miller, C. Muus, M. Niemi, R. Padera, L. Pan, D. Pant, C. Pe'er, J. Pfiffner-Borges, C. J. Pinto, J. Plaisted, J. Reeves, M. Ross, M. Rudy, E. H. Rueckert, M. Siciliano, A. Sturm, E. Todres, A. Waghray, S. Warren, S. Zhang, D. R. Zollinger, L. Cosimi, R. M. Gupta, N. Hacohen, H. Hibshoosh, W. Hide, A. L. Price, J. Rajagopal, P. R. Tata, S. Riedel, G. Szabo, T. L. Tickle, P. T. Ellinor, D. Hung, P. C. Sabeti, R. Novak, R. Rogers, D. E. Ingber, Z. G. Jiang, D. Juric, M. Babadi, S. L. Farhi, B. Izar, J. R. Stone, I. S. Vlachos, I. H. Solomon, O. Ashenberg, C. B. M. Porter, B. Li, A. K. Shalek, A. C. Villani, O. Rozenblatt-Rosen, A. Regev, COVID-19 tissue atlases reveal SARS-CoV-2 pathology and cellular targets. *Nature* **595**, 107–113 (2021).
89. C. Wang, L. Chen, Y. Chen, W. Jia, X. Cai, Y. Liu, F. Ji, P. Xiong, A. Liang, R. Liu, Y. Guan, Z. Cheng, Y. Weng, W. Wang, Y. Duan, D. Kuang, S. Xu, H. Cai, Q. Xia, D. Yang, M. W. Wang, X. Yang, J. Zhang, C. Cheng, L. Liu, Z. Liu, R. Liang, G. Wang, Z. Li, H. Xia, T. Xia, Abnormal global alternative RNA splicing in COVID-19 patients. *PLOS Genet.* **18**, e1010137 (2022).
90. A. K. Banerjee, M. R. Blanco, E. A. Bruce, D. D. Honson, L. M. Chen, A. Chow, P. Bhat, N. Ollikainen, S. A. Quinodoz, C. Loney, J. Thai, Z. D. Miller, A. E. Lin, M. M. Schmidt, D. G. Stewart, D. Goldfarb, G. de Lorenzo, S. J. Rihn, R. M. Voorhees, J. W. Botten, D. Majumdar, M. Guttman, SARS-CoV-2 disrupts splicing, translation, and protein trafficking to suppress host defenses. *Cell* **183**, 1325–1339.e21 (2020).
91. L. Zhuang, L. Lu, R. Zhang, K. Chen, X. Yan, Comprehensive integration of single-cell transcriptional profiling reveals the heterogeneities of non-cardiomyocytes in healthy and ischemic hearts. *Front. Cardiovasc. Med.* **7**, 615161 (2020).

92. K. Kanemaru, J. Cranley, D. Muraro, A. M. A. Miranda, S. Y. Ho, A. Wilbrey-Clark, J. Patrick Pett, K. Polanski, L. Richardson, M. Litvinukova, N. Kumasaka, Y. Qin, Z. Jablonska, C. I. Semprich, L. Mach, M. Dabrowska, N. Richoz, L. Bolt, L. Mamanova, R. Kapuge, S. N. Barnett, S. Perera, C. Talavera-López, I. Mulas, K. T. Mahbubani, L. Tuck, L. Wang, M. M. Huang, M. Prete, S. Pritchard, J. Dark, K. Saeb-Parsy, M. Patel, M. R. Clatworthy, N. Hübner, R. A. Chowdhury, M. Noseda, S. A. Teichmann, Spatially resolved multiomics of human cardiac niches. *Nature* **619**, 801–810 (2023).
93. K. M. Sitnik, K. Wendland, H. Weishaupt, H. Uronen-Hansson, A. J. White, G. Anderson, K. Kotarsky, W. W. Agace, Context-dependent development of lymphoid stroma from adult CD34⁺ adventitial progenitors. *Cell Rep.* **14**, 2375–2388 (2016).
94. K. R. Stenmark, M. E. Yeager, K. C. el Kasmi, E. Nozik-Grayck, E. V. Gerasimovskaya, M. Li, S. R. Riddle, M. G. Frid, The adventitia: Essential regulator of vascular wall structure and function. *Annu. Rev. Physiol.* **75**, 23–47 (2013).
95. M. Corselli, C. W. Chen, B. Sun, S. Yap, J. P. Rubin, B. Péault, The tunica adventitia of human arteries and veins as a source of mesenchymal stem cells. *Stem Cells Dev.* **21**, 1299–1308 (2012).
96. M. W. Dahlgren, S. W. Jones, K. M. Cautivo, A. Dubinin, J. F. Ortiz-Carpena, S. Farhat, K. S. Yu, K. Lee, C. Wang, A. V. Molofsky, A. D. Tward, M. F. Krummel, T. Peng, A. B. Molofsky, Adventitial stromal cells define group 2 innate lymphoid cell tissue niches. *Immunity* **50**, 707–722.e6 (2019).
97. D. Park, J. A. Spencer, B. I. Koh, T. Kobayashi, J. Fujisaki, T. L. Clemens, C. P. Lin, H. M. Kronenberg, D. T. Scadden, Endogenous bone marrow MSCs are dynamic, fate-restricted participants in bone maintenance and regeneration. *Cell Stem Cell* **10**, 259–272 (2012).
98. V. W. Yu, D. T. Scadden, Heterogeneity of the bone marrow niche. *Curr. Opin. Hematol.* **23**, 331–338 (2016).
99. W. Gu, Z. Ni, Y. Q. Tan, J. Deng, S. J. Zhang, Z. C. Lv, X. J. Wang, T. Chen, Z. Zhang, Y. Hu, Z. C. Jing, Q. Xu, Adventitial cell atlas of wt (wild type) and ApoE (apolipoprotein E)-deficient mice defined by single-cell RNA sequencing. *Arterioscler. Thromb. Vasc. Biol.* **39**, 1055–1071 (2019).

100. G. Díaz-Araya, R. Vivar, C. Humeres, P. Boza, S. Bolivar, C. Muñoz, Cardiac fibroblasts as sentinel cells in cardiac tissue: Receptors, signaling pathways and cellular functions. *Pharmacol. Res.* **101**, 30–40 (2015).
101. J. T. Rodgers, M. D. Schroeder, C. Ma, T. A. Rando, HGFA is an injury-regulated systemic factor that induces the transition of stem cells into GAlert. *Cell Rep.* **19**, 479–486 (2017).
102. N. G. Frangogiannis, The inflammatory response in myocardial injury, repair, and remodelling. *Nat. Rev. Cardiol.* **11**, 255–265 (2014).
103. M. J. Ivey, J. T. Kuwabara, J. T. Pai, R. E. Moore, Z. Sun, M. D. Tallquist, Resident fibroblast expansion during cardiac growth and remodeling. *J. Mol. Cell. Cardiol.* **114**, 161–174 (2018).
104. D. Jeong, M. A. Lee, Y. Li, D. K. Yang, C. Kho, J. G. Oh, G. Hong, A. Lee, M. H. Song, T. J. LaRocca, J. Chen, L. Liang, S. Mitsuyama, V. D'Escamard, J. C. Kovacic, T. H. Kwak, R. J. Hajjar, W. J. Park, Matricellular protein CCN5 reverses established cardiac fibrosis. *J. Am. Coll. Cardiol.* **67**, 1556–1568 (2016).
105. A. Hillsley, M. S. Santoso, S. M. Engels, K. N. Halwachs, L. M. Contreras, A. M. Rosales, A strategy to quantify myofibroblast activation on a continuous spectrum. *Sci. Rep.* **12**, 12239 (2022).
106. T. B. Layton, L. Williams, H. Colin-York, F. E. McCann, M. Cabrita, M. Feldmann, C. Brown, W. Xie, M. Fritzsche, D. Furniss, J. Nanchahal, Single cell force profiling of human myofibroblasts reveals a biophysical spectrum of cell states. *Biol. Open* **9**, bio049809 (2020).
107. C. Humeres, A. V. Shinde, A. Hanna, L. Alex, S. C. Hernández, R. Li, B. Chen, S. J. Conway, N. G. Frangogiannis, Smad7 effects on TGF- β and ErbB2 restrain myofibroblast activation and protect from postinfarction heart failure. *J. Clin. Invest.* **132**, e146926 (2022).
108. R. Vivar, C. Humeres, R. Anfossi, S. Bolivar, M. Catalán, J. Hill, S. Lavandero, G. Diaz-Araya, Role of FoxO3a as a negative regulator of the cardiac myofibroblast conversion induced by TGF- β 1. *Biochim. Biophys. Acta Mol. Cell Res.* **1867**, 118695 (2020).

109. B. Hinz, D. Lagares, Evasion of apoptosis by myofibroblasts: A hallmark of fibrotic diseases. *Nat. Rev. Rheumatol.* **16**, 11–31 (2020).
110. J. D. Lanzer, L. M. Wienecke, R. O. Ramirez-Flores, M. M. Zylla, N. Hartmann, F. Sicklinger, J.-H. Schultz, N. Frey, J. Saez-Rodriguez, F. Leuschner, Single-cell transcriptomics reveal distinctive patterns of fibroblast activation in murine heart failure with preserved ejection fraction. *bioRxiv* 2023.05.09.539983 [Preprint] (2023). <https://doi.org/10.1101/2023.05.09.539983>.
111. D. Tong, G. G. Schiattarella, N. Jiang, F. Altamirano, P. A. Szweda, A. Elnwasany, D. I. Lee, H. Yoo, D. A. Kass, L. I. Szweda, S. Lavandero, E. Verdin, T. G. Gillette, J. A. Hill, NAD⁺ repletion reverses heart failure with preserved ejection fraction. *Circ. Res.* **128**, 1629–1641 (2021).
112. M. Abdellatif, V. Trummer-Herbst, F. Koser, S. Durand, R. Adão, F. Vasques-Nóvoa, J. K. Freundt, J. Voglhuber, M. R. Pricolo, M. Kasa, C. Türk, F. Aprahamian, E. Herrero-Galán, S. J. Hofer, T. Pendl, L. Rech, J. Kargl, N. Anto-Michel, S. Ljubojevic-Holzer, J. Schipke, C. Brandenberger, M. Auer, R. Schreiber, C. N. Koyani, A. Heinemann, A. Zirlik, A. Schmidt, D. von Lewinski, D. Scherr, P. P. Rainer, J. von Maltzahn, C. Mühlfeld, M. Krüger, S. Frank, F. Madeo, T. Eisenberg, A. Prokesch, A. F. Leite-Moreira, A. P. Lourenço, J. Alegre-Cebollada, S. Kiechl, W. A. Linke, G. Kroemer, S. Sedej, Nicotinamide for the treatment of heart failure with preserved ejection fraction. *Sci. Transl. Med.* **13**, eabd7064 (2021).
113. E. Boileau, X. Li, I. S. Naarmann-de Vries, C. Becker, R. Casper, J. Altmüller, F. Leuschner, C. Dieterich, Full-length spatial transcriptomics reveals the unexplored isoform diversity of the myocardium post-MI. *Front. Genet.* **13**, 912572 (2022).
114. S. L. Wolock, R. Lopez, A. M. Klein, Scrublet: Computational identification of cell doublets in single-cell transcriptomic data. *Cell Syst.* **8**, 281–291.e9 (2019).
115. Z. Gu, R. Eils, M. Schlesner, Complex heatmaps reveal patterns and correlations in multidimensional genomic data. *Bioinformatics* **32**, 2847–2849 (2016).
116. M. N. Wright, A. Ziegler, ranger: A fast implementation of random forests for high dimensional data in C++ and R. *J. Stat. Softw.* **77**, 1–17 (2017).

117. F. A. Wolf, P. Angerer, F. J. Theis, SCANPY: Large-scale single-cell gene expression data analysis. *Genome Biol.* **19**, 15 (2018).
118. M. I. Love, W. Huber, S. Anders, Moderated estimation of fold change and dispersion for RNA-seq data with DESeq2. *Genome Biol.* **15**, 550 (2014).
119. B. Klaus, K. Strimmer, *fdrtool: Estimation of (Local) False Discovery Rates and Higher Criticism* (The Comprehensive R Archive Network, 2021).
120. D. Risso, J. Ngai, T. P. Speed, S. Dudoit, Normalization of RNA-seq data using factor analysis of control genes or samples. *Nat. Biotechnol.* **32**, 896–902 (2014).
121. A. Brionne, A. Juanchich, C. Hennequet-Antier, ViSEAGO: A Bioconductor package for clustering biological functions using Gene Ontology and semantic similarity. *BioData Min.* **12**, 16 (2019).
122. S. Durinck, Y. Moreau, A. Kasprzyk, S. Davis, B. de Moor, A. Brazma, W. Huber, BioMart and Bioconductor: A powerful link between biological databases and microarray data analysis. *Bioinformatics* **21**, 3439–3440 (2005).
123. A. Alexa, J. Rahnenfuhrer, *topGO: Enrichment Analysis for Gene Ontology* (Bioconductor, 2022).
124. L. Garcia-Alonso, C. H. Holland, M. M. Ibrahim, D. Turei, J. Saez-Rodriguez, Benchmark and integration of resources for the estimation of human transcription factor activities. *Genome Res.* **29**, 1363–1375 (2019).
125. R. Kolde, *pheatmap: Pretty Heatmaps* (The Comprehensive R Archive Network, 2019).
126. B. Phipson, C. B. Sim, E. R. Porrello, A. W. Hewitt, J. Powell, A. Oshlack, propeller: Testing for differences in cell type proportions in single cell data. *Bioinformatics* **38**, 4720–4726 (2022).
127. D. W. McKellar, L. D. Walter, L. T. Song, M. Mantri, M. F. Z. Wang, I. de Vlaminck, B. D. Cosgrove, Large-scale integration of single-cell transcriptomic data captures transitional progenitor states in mouse skeletal muscle regeneration. *Commun. Biol.* **4**, 1280 (2021).

128. L. Ting, R. Rad, S. P. Gygi, W. Haas, MS3 eliminates ratio distortion in isobaric multiplexed quantitative proteomics. *Nat. Methods* **8**, 937–940 (2011).
129. S. E. Iismaa, M. Li, S. Kesteven, J. Wu, A. Y. Chan, S. R. Holman, J. W. Calvert, A. U. Haq, A. M. Nicks, N. Naqvi, A. Husain, M. P. Feneley, R. M. Graham. Cardiac hypertrophy limits infarct expansion after myocardial infarction in mice. *Sci. Rep.* **8**, 6114 (2018).
130. A. O. Ward, V. Janbandhu, G. Chapman, S. L. Dunwoodie, R. P. Harvey. An image analysis protocol using cellprofiler for automated quantification of post-ischemic cardiac parameters. *STAR Protoc.* **3**, 101097 (2022).
131. O. Contreras, R. P. Harvey. Single-cell transcriptome dynamics of the autotaxin-lysophosphatidic acid axis during muscle regeneration reveal proliferative effects in mesenchymal fibro-adipogenic progenitors. *Front. Cell Dev. Biol.* **11**, 1017660 (2023).